Analysis of microstructural strain-fields in grey cast iron

by

David P.B. Samuelsson

Diploma work No. 47/2011

at Department of Materials and Manufacturing Technology

CHALMERS UNIVERSITY OF TECHNOLOGY

Göteborg, Sweden

Diploma work in the Master program Advanced engineering materials

Performed at: **SP Technical Research Institute of Sweden**
Building Technology and Mechanics

P.O. Box 857, SE-501 15 Borås, Sweden

Supervisor(s): PhD Torsten Sjögren
SP Technical Research Institute of Sweden
P.O. Box 857, SE-501 15 Borås, Sweden

Examiner: Professor Maria Knutson Wedel
Department of Materials and Manufacturing Technology
Chalmers University of Technology, SE-412 96 Göteborg

Analysis of microstructural strain-fields in grey cast iron

David Samuelsson

Diploma work no 47/2011

Department of Materials and Manufacturing Technology

Chalmers University of Technology

SE-412 96 Göteborg

Sweden

Telephone + 46 (0)31-772 1000

Cover image:

Strain-field of a color-etched microstructure.
Reproservice Chalmers
Göteborg, Sweden 2011

Analysis of microstructural strain-fields in grey cast iron

David Samuelsson

Department of Materials and Manufacturing Technology

Chalmers University of Technology

Abstract

With increasing engine capacity the demand on the material increases. To meet the requirements new more advanced test methods are invented. One of these test methods is the digital image correlation technique (DIC). This method analyses deformations in materials by correlating the displacement in a set of sequentially acquired images. To be able to measure the deformations the material needs to have a distinct pattern. Some materials have a "natural" pattern, e.g. the etched microstructure of grey cast iron, other materials needs to get an artificial pattern which is done by spraying with a substance that disperses onto the surface and results in different contrasts.
A new way to utilize this technique is to use a microscope viewing the surface, and collect images and analyze them with a DIC software. This gives information about the local strain-field of the material.
In metals different patterns can be achieved depending on what etchant is used. This means that it is possible to differentiate local strains between different phases of the studied material. For a gray cast iron etched with alkaline sodium picrate (a color etchant which highlights eutectic cells) it is possible to detect local strains in and around these cells. Analyzes showed that the highest strains could be found in the graphite followed by pearlite. For a microstructure with revealed eutectic cells the highest strains could be seen inside the eutectic cells for larger cells. Materials with large cells showed worse global mechanical properties than materials with small cells.

The difficulties with the DIC-method is that it is sensitive to contrasts and since contrast are affected by e.g. vibrations, shiny surfaces and surfaces with small contrast difference it can be hard to get quantitative answers.

Digital image correlations techniques have shown to be an instrument of the future in analyzing microscopic strains. By knowing how the different phases accommodate strains and how changes in the microstructure, due to melt treatment and alloying, affect the strain-field the DIC-method can be used as a powerful tool in future material modeling.

Keywords: Grey cast iron, eutectic cells, strain fields, graphite, digital image correlation, DIC

Contents

1 Introduction

CHAPTER INTRODUCTION

This chapter aims to introduce the scope and the problem of the thesis work. It also points out the limitations of this work and summarizes the structure of the report.

1.1 Project background

The use of digital image correlation techniques (DIC) is becoming more common as the computers and the digital cameras are improving their performance. The technique uses images taken at different load and elongation. By comparing subsequent images with the strain-free first image it is possible to determine the displacements in different parts of the materials structure. For the DIC to be able to perform the displacement analysis a contrast difference is demanded within the pattern. The pattern can be a natural pattern e.g. the microstructure of an etched grey cast iron or a substance that is sprayed on the material to make a pattern. An advantage with this is that it gives information about local deformations not only the mean value over a surface. One example can be how the local strains are affected by a weld.

SP Technical Research Institute of Sweden has a DIC software and equipment called (ARAMIS^{TM}) which is a non contact method for measuring deformations. This method is mostly used for determination of strains on a macroscopic level e.g. testing of a tensile test piece or any other test piece or component that is exposed to a load. During recent time it has also been used on a microscopic scale level, where a microscope has been used to capture images of the microstructure.

In this thesis microstructural strains are investigated in a color etched gray cast iron. With this method it should be possible to analyze strain-fields around and at the so called eutectic cells that are visible after color etching. The microstructural strain-fields will be compared with globally measured strains, to increase the knowledge of the materials macroscopic deformation behavior. Some investigations on static and dynamic properties will also be performed to further increase the knowledge of the material.

1.2 Purpose

The aim of this project is to study the limitations and possibilities of the DIC method for measurements on a microstructural level. The method is used on gray cast iron to investigate the microstructural strain-fields. In addition to this the dependence of the different microstructural parameters, such as eutectic cells, chemical composition and mechanical properties of the material are investigated.

1.3 Environmental aspects

Global warming is, according to many scientists, caused by the burning of fossil fuels which forms greenhouse gases. One of these gases is carbon dioxide (CO_2), which is thought to be the main problem. Carbon dioxide is not the most potential greenhouse gas, but is the gas emitted to the largest extent. The reason for this is that all fossil fuels contain carbon chains, which forms CO_2 during combustion. Diesel engines are thus one of the sources of CO_2 emissions in the world.

All large diesel engines have grey cast iron as their main material. Grey cast iron is a material that is suited very well for large engines but has limitations regarding the mechanical properties. By improving the strength of the grey iron materials the engine producing companies can increase the combustion pressure of the engines. This leads to higher efficiency, which means less energy for the same amount of work. By this it can be concluded that both fuel consumption and the amount of emissions would be lowered.

This is one of the reasons why science is carried out in the materials field and is one of the reasons for this project.

1.4 Structure and limitations of the report

This thesis work is limited to 20 weeks. From a test series of seven different grey iron materials, a set of samples were investigated regarding its microstructure, mechanical properties and the relation to how strain are accommodated within the material on a microstructural level.

The report background contains brief reviews on: Grey cast iron, Mechanical properties, statistics and digital image correlation. It is done in this way to facilitate for the reader, regardless of his/her experience level. The report continues with a description of the used experimental methods and ends with a presentation of results and conclusions.

2 Grey cast iron

CHAPTER INTRODUCTION

This chapter is intended to give basic background information to grey cast iron, how the microstructure is defined, the terminology and material properties. The focus will be on grey cast iron issues that concerns the thesis work.

The carbon content in an iron-carbon alloy is what essentially differentiates cast iron from steel. If the carbon content exceeds 2.0 wt% the alloy is considered as cast iron. When the amount of carbon (given in weight percent) in grey cast iron is lower than the eutectic composition (4.3 wt%) the materials are denominated hypoeutectic. The order in which the different phases and compounds form at decreasing temperature for a hypoeutectic composition can be seen along the blue dotted line in Figure 1. The content of chapter 2 follows the order of formation as indicated in Figure 1.

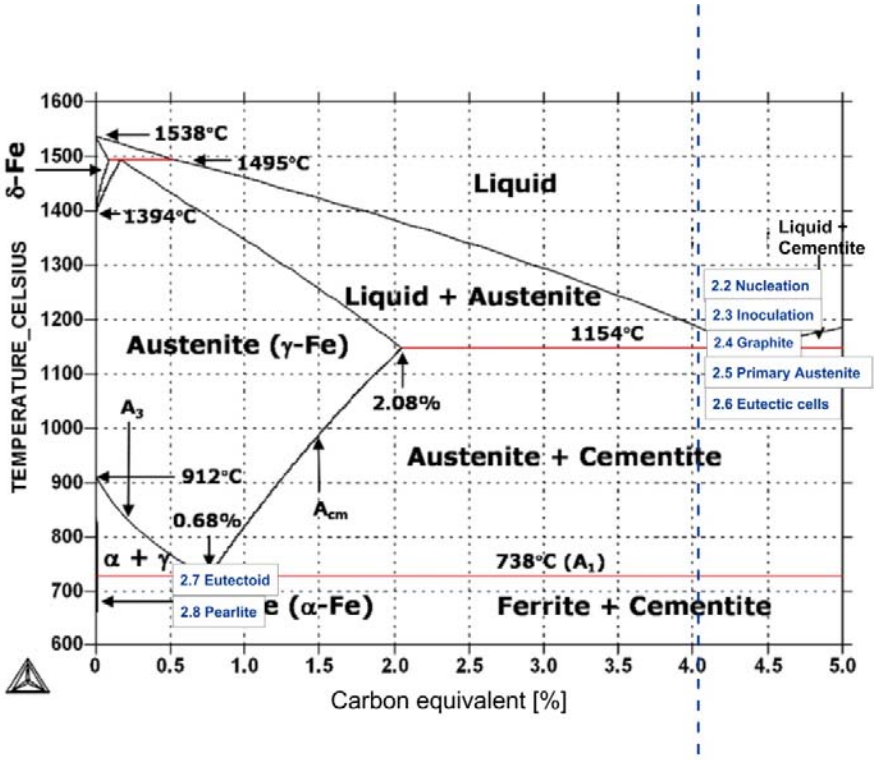

Figure 1. Metastable iron - carbon phase diagram with chapter events following the indicated blue line.

2.1 Alloying elements

Alloying elements are added to the melt to control and change the properties of the material. Different alloying elements affect the microstructure in different ways. For grey cast iron the most important alloying elements are carbon (C) and silicon (Si), (1). The effect of other alloying elements are also described below, but extra focus will be set on chromium (Cr), copper (Cu) and nitrogen (N) since they are intentionally altered in the materials studied in this thesis work.

Grey iron contains many alloying elements. In addition to C and Si mentioned above, it also contains elements like e.g. phosphorus (P), nickel (Ni), tin (Sn), copper, chromium and manganese (Mn). Since all

alloying elements change the microstructure and the phases that form, the phase diagrams becomes very complex. To make a good approximation of the multiphase system, a more precise diagram than the iron-carbon diagram and a less complicated than a multiphase diagram is needed. To achieve this, the carbon equivalence (CE) is used. CE is an approximation taking into account the amount of carbon, silicon and phosphorus as main affecting elements. The CE is a binary approximation of a multiphase diagram as depicted in Figure 2, (2). CE is calculated according to Equation 1.

$$CE = \%C + \frac{\%Si + \%P}{3} \qquad \textbf{Equation 1}$$

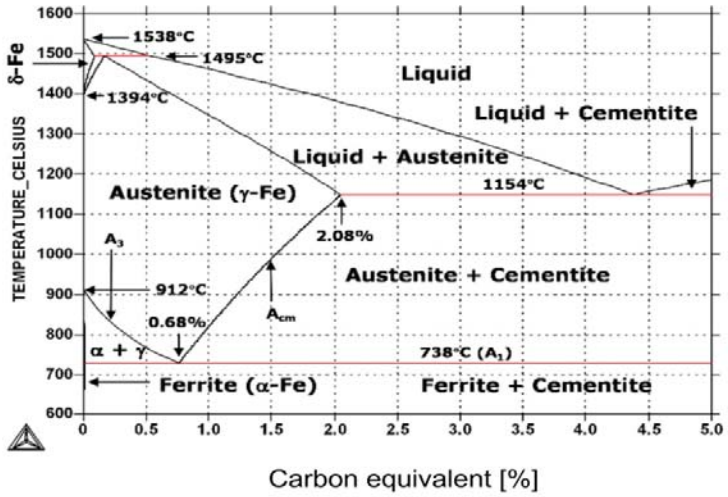

Figure 2. Metastable iron-carbon phase diagram.

Alloying elements does not only change the microstructure in one way, it can react with other alloying elements and change the microstructure in several ways. The elements might also have different influence at the eutectic and eutectoid reaction. General features that can be concluded for the specific alloying elements are listed in Table1.

The eutectoid transformation is affecting the mechanical properties the most and is therefore a very important factor to control. All alloying elements affect the final microstructure but due to the focus in this thesis work Cu, Cr and N will be discussed further.

Tab1e 1. Effect of different alloying elements during solidification (3).

Element	Effect during eutectic solidification	Effect during eutectoid reaction
Aluminum	Strong graphitizer	Promotes ferrite and graphite formation
Chromium	Strong carbide former. Forms complex carbides which are very stable.	Strong pearlite former
Copper	Mild graphitizer	Promotes pearlite formation
Molybdenum	Mild carbide former	Strong pearlite promoter
Nickel	Graphitizer	Mild pearlite promoter
Phosphorus	Promotes steadite formation	The information of phosphorus effects during eutectoid is obscure
Silicon	Strong graphitizer	Promotes ferrite and graphite formation
Tin	Little effect with amount used	Strong pearlite retainer
Titanium under 0.25%	Graphitizer	Promotes graphite formation
Vanadium	Strong carbide former	Strong pearlite former

Chromium

Chromium raises the eutectoid temperature and facilitates the formation of a homogeneous material.
It is a pearlite promoter and less than 0.4% is needed to increase the pearlite content. If the concentration exceeds 0.4% it forms meta-stable carbide precipitates instead. This is also depending on the C, Si and amount of inoculation (see Inoculants 2.3).
An addition of Cr makes graphite flakes shorter and thinner. And it is easier to achieve a homogeneous material (4).

Copper

Cu reduces eutectic cell size, increases the number of eutectic cells, stabilizes pearlite and coarsens graphite. For a base iron composition it has been shown that Cu increases the tensile strength with concentration up to 0.35 %. Excessive amounts give less effect on strength increase (5).
Another source says that the surface area of the graphite is decreased by Cu additions but the length increases, which are contradictory to the previous statement (4).

Nitrogen

A common problem when using nitrogen is blowhole defects. This is an effect of the decreasing solubility of nitrogen in the melt. For this reason local high concentrations of nitrogen arise, in which gas holes may form (6). N is affecting the graphite length by shortening it, which leads to an increase in hardness of the material (7).

2. 2 Nucleation

Undercooling

To grasp the nucleation concept it is necessary to understand the model of undercooling.

Undercooling occurs when the temperature is below the melting point of the liquid. This means that the difference in Gibb's free energy between the liquid and the solid phase at this low temperature is the driving force for solidification. To be able to quantify the undercooling an assumption is made which says; there is no difference in specific heat of the liquid and the solid. With that assumption and the knowledge that the difference in Gibbs free energy is zero at the melting point it is possible to describe the undercooling as:

$$\Delta G = \frac{L\Delta T}{T_m} \qquad \textbf{Equation 2}$$

Where L is the latent heat of sublimation, ΔT the undercooling and T_m the melting temperature (8).

Nucleation

There are two kinds of nucleation of solids in liquid possible; homogeneous and heterogeneous. The difference is if there exist surfaces for nucleation or not. Since surfaces exist, as present by the added inoculants, heterogeneous nucleation is discussed in this section. The effect from having a surface lowers the demands on undercooling, which will be shown.

The expression for energy changes during formation of a solid can be derived with the expression (8):

$$\Delta G_{het} = -V_s \Delta G_v + A_{SL}\gamma_{SL} + A_{SM}\gamma_{SM} + A_{SM}\gamma_{ML} \qquad \textbf{Equation 3}$$

Where V_s is the volume of the formed solid, ΔG_v is the volume free energy of formation (see undercooling), A the area and the indexes S, L and M represents liquid, solid and mould.

If the interfacial free energies are described by:

$$\gamma_{ML} = \gamma_{SM+}\gamma_{SL}\cos\theta \qquad \textbf{Equation 4}$$

This can be combined with Equation 3 to form:

$$\Delta G_{het} = \left\{-\frac{4}{3}\pi r^3 \Delta G_v + 4\pi r^2 \gamma_{SL}\right\} S(\theta) \qquad \textbf{Equation 5}$$

Where; $S(\theta) = \frac{(2+\cos\theta)(1-\cos\theta)^2}{4}$

These can be composed to a diagram as shown in Figure 3.

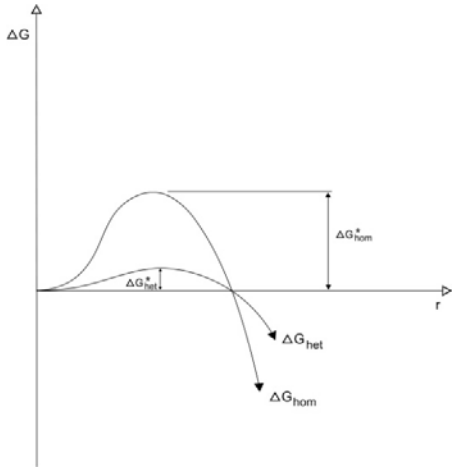

Figure 3. The difference between homogeneous and heterogeneous nucleation. The star (*) is an index for the critical value (for ΔG it is called the activation energy). As can be seen the heterogeneous nucleation has lower activation energy than the homogeneous.

From Figure 3 it can be seen that the homogeneous activation energy is larger than the heterogeneous for the same radius. This variation shows the difference between the required undercooling for heterogeneous and homogeneous nucleation. The smaller activation energy, the smaller the demand on temperature differences is.

2.3 Inoculants

Inoculants are used to promote nucleation (see nucleation above) of graphite, which leads to formation of eutectic cells. For effective inoculation the lattice of the inoculants should match the lattice of the solid that is to be formed. A good lattice match lowers the Gibbs free energy. These effects can be seen by plotting the deviation from crystal lattice with the undercooling (9). Since the undercooling can be kept low at effective inoculation type A graphite is promoted (10). ASM Metal Handbook (2) describes it as "to promote the formation of crystals on a nucleant, the interface between the nucleant and the liquid should be of higher energy than that between the nucleant and the crystal solid", which summarizes it in a good way.

Thus, the addition of inoculant lowers the needed undercooling by increasing the number of available nucleation sites.

The used inoculant for the materials analyzed in the thesis work is Foundrisil75. This is an inoculant that is especially designed for grey irons with low sulphur content, where other inoculants are less effective due to their lack of stable compositions over different sizes. The most important effect of Foundrisil is that it reduces chill and that it forms less dross (11).

2.4 Graphite

Carbon which forms graphite is the main alloying element in cast iron. Carbon is a small atom which means that it follows the "fast" interstitial diffusion model. As the diffusion proceeds, graphite forms. The graphite provides many beneficial effects like e.g. thermal conductivity and wear resistance; these effects are found to be very good in e.g. engine applications.

Graphite has a hexagonal structure with strong covalent bonds in the plane (A-direction), (see Figure 4). Therefore, when melting cast iron the only thing that will remain is the submicroscopic grains (small particles of graphite that has stable carbon-carbon covalent bonds). These are good initial sites for creating new graphite (12).

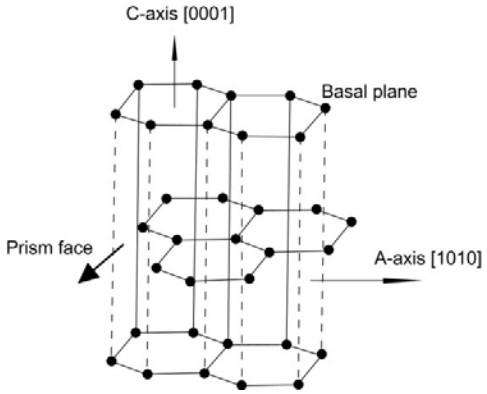

Figure 4. Crystallographic structure of graphite.

For grey iron, the properties differ with shape, size, amount and distribution of the graphite flakes (mainly flakes but some other forms may exist). The graphite phase can be categorized regarding its distribution. For the distribution this is done by dividing it into A-E as shown in Figure 5, (2). These different distributions are products of different undercooling (see nucleation) and alloying content.

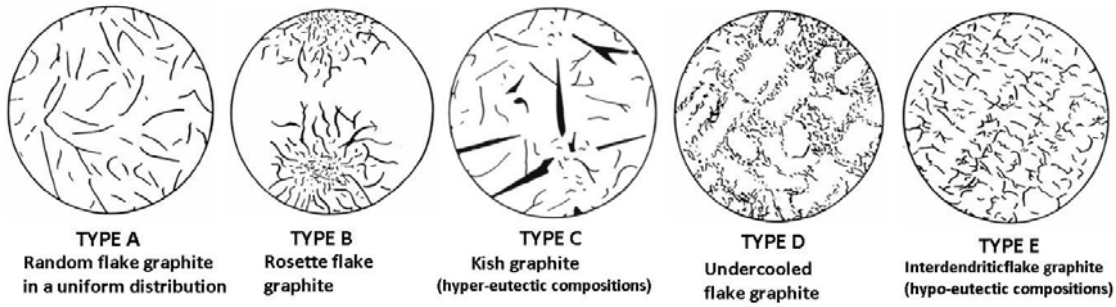

Figure 5. Showing different types of flake graphite following EN ISO 945 (13).

Since the graphite phase is much softer than the surrounding matrix it is often seen as voids at e.g. micro mechanical modeling. These voids together with the interconnection of the flakes make graphite the main influence on mechanical properties of grey cast iron. To prevent the material from being too weak, formation of a pearlitic matrix with graphite particles ordered in a way to prevent continuous cracking is necessary (Table 2 and Table 3).The pearlitic grey iron structure has very good compressive strength, vibration damping and thermal conductivity (3). For these reasons the pearlitic grey cast irons are suitable for the use in engine components.

Table 2. Grey cast iron hardness for different matrices (2).

Microstructure	Hardness, HB
Ferrite + graphite	110-140
Pearlite + graphite	200-260
Bainite + graphite	260-350
Austenite + graphite	140-160

Depending on the type of graphite the mechanical properties varies a lot. For this reason Table 2 only shows hardness (not tensile strength) for the different microstructures. There is a correlation between hardness and tensile strength that says: as the hardness increases the strength increases and the elongation decreases. This is presented for the individual phases in Table 3.

Table 3. Comparison between phases, tensile, elongation and hardness (2).

Phase	Tensile strength, MPa	Elongation %	Hardness, HB
Pearlite	862	10	200
Ferrite	272-290	61	75

2.5 Primary austenite

The first solid to form in grey cast iron is the primary austenite. The growth is dendritic with equiaxed and/or columnar crystals see Figure 6, (13).

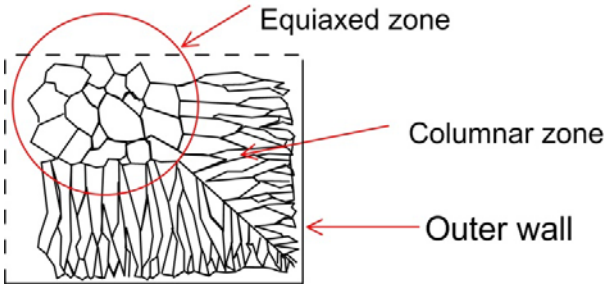

Figure 6. Columnar and equiaxed crystals.

For the austenite dendrites to grow in a binary fluid a constitutional supercooling is demanded, as seen in Figure 7, i.e., the actual temperature (T_L) has to have a lower gradient than the equilibrium temperature (T_e), (13),(8). This is possible due to inadequate diffusion away from the interface, which creates a concentration gradient that forms a new equilibrium temperature curve. (Since the undercooling gradient arises from the composition, it is denominated constitutional).

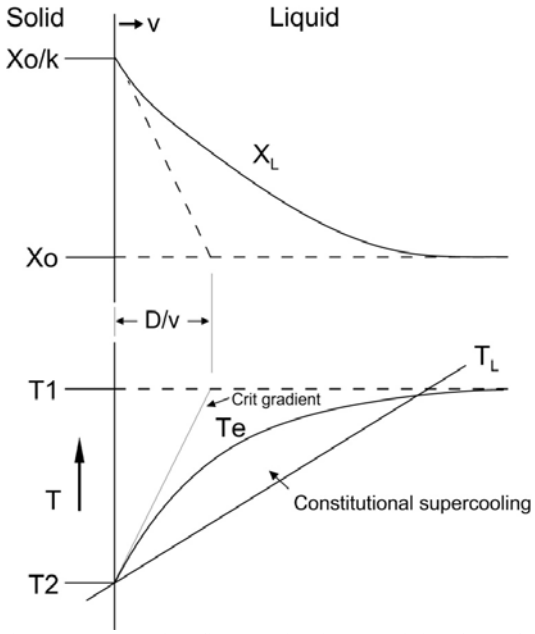

Figure 7. Shows the constitutional supercooling field, which is the driving force for the dendritic growth. X_L is the concentration gradient that is formed in front of the solid interface, T_E is the equilibrium temperature formed in the liquid due to the concentration gradient and T_L is the actual temperature of the liquid.

Hypoeutectic compositions can grow in other forms than dendrites but rarely does (14). This can be explained from Figure 7, as the actual temperature (T_L) needs to be below the equilibrium temperature (T_e) for the composition to grow as dendrites. So for the composition to grow as a planar, the temperature would

need to be higher or equal to the critical gradient. This means no undercooling and the protrusions would melt back. This reasoning is valid during steady state forming.

To change the dendritic size different inoculants can be used, which changes the cooling time. Analyses show how the equiaxed dendrites change compared to eutectic cells for different or no inoculants. The inoculated material increased its dendritic size but kept its eutectic cell size while the non-inoculated material increased both. If pure iron powder were used the eutectic cells were increased but the dendrites kept small (15).

2.6 Eutectic cells

Subsequent to the formation of the primary austenite, graphite is formed which leads to iron rich zones. The graphite and the iron rich zones then form eutectic cells, which are not affected by the primary austenite (but strongly depend on different alloying elements).

Thus, eutectic cells are a mixture of austenite and graphite. At the solid state transformation (eutectoid transformation) the austenite transforms into ferrite and cementite or graphite. The phase diagram (Figure 2) only shows the metastable phase diagram and for that reason no information on the transformation into graphite is present. The transformations that occur depend on the systems stability. If the system is stable it prefers graphite while the metastable prefer cementite as the carbon rich phase. The stable system is the equilibria between iron and graphite while the metastable is between Fe and cementite, (16). The eutectic cells are together with pearlite the main constituents of grey iron. The number and size of the eutectic cells affect the properties to a great extent where especially fatigue properties are reported to be strongly affected (12).

Throughout the solidification and solid state transformation the austenite in the eutectic becomes continuous with the dendritic proeutectic austenite. For this reason it is impossible to distinguish the eutectic cell structure and the proeutectic austenite dendrites with an ordinary light optical microscope. To make a distinction between the austenite in the microstructure, etching is necessary (1). Such etched microstructure of a grey iron is seen in Figure 8.

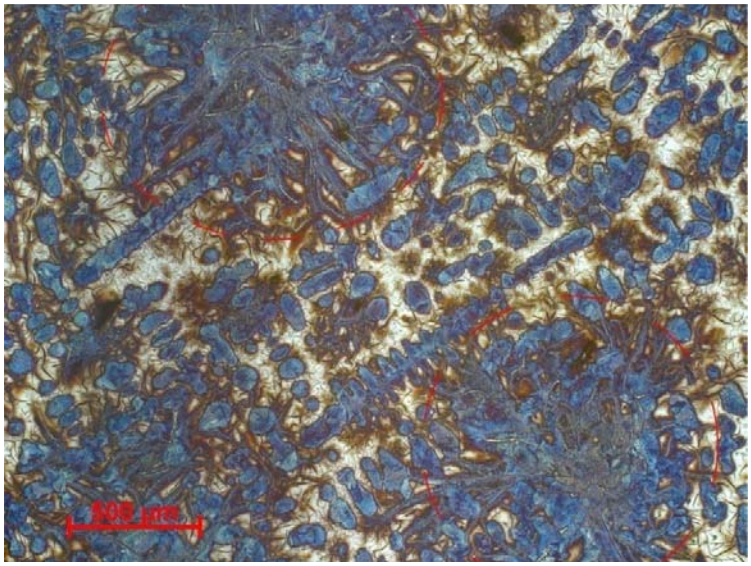

Figure 8. Microstructure showing eutectic cells (marked with red circles for clarification). Courtesy to Fredrik Wilberfors, Scania CV AB.

The appearance of the eutectic cells is mainly influenced by (17):

- Chemical composition
- Inoculation
- Cooling rate

2.7 Eutectoid

As mentioned in 2.6; subsequent to eutectic reaction a eutectoid transformation takes place.
It is the point where one solid phase transforms into two new solid phases (in comparison a eutectic instead transforms from liquid), (18).

For the metastable system (non equilibrium) the eutectoid composition is around 0.8 wt% C and the austenite (γ) is transformed into cementite and ferrite (α), (pearlite). Similarly, the austenite transforms into graphite and ferrite for the stable system.

2.8 Pearlite

Pearlite (see Figure 9 and Figure 10) is a microstructural constituent that is hard and has high strength. It is a combination of ferrite and cementite and has a lamellar appearance. The mechanical properties of pearlite strongly depend on the lamellar spacing and as the spacing increases the strength decreases (19).

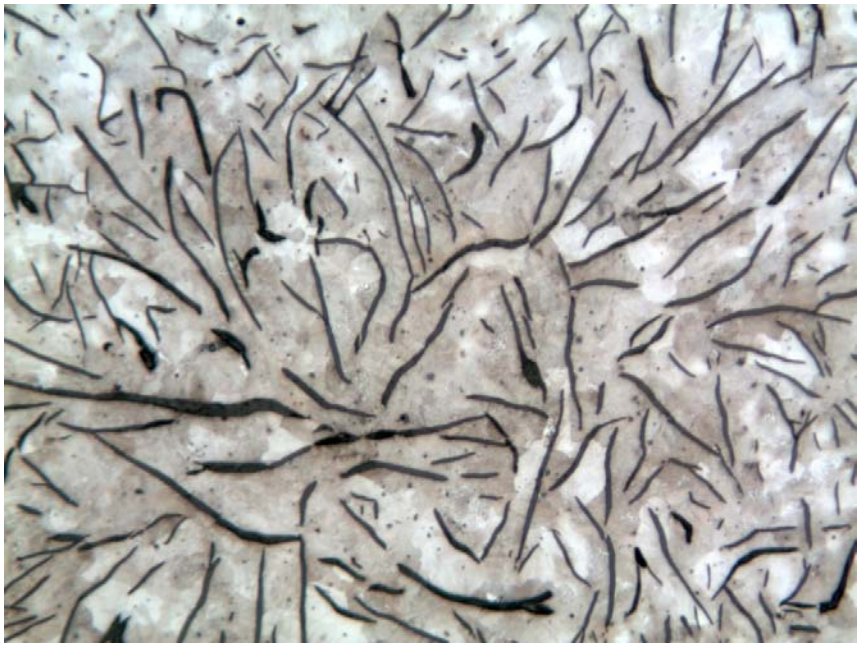

Figure 9. Microstructure showing graphite (black areas) surrounded by pearlite. The pearlite appears in different colors due to different cutting angles of the lamellas. This means that both grey/brown areas and white are pearlite.

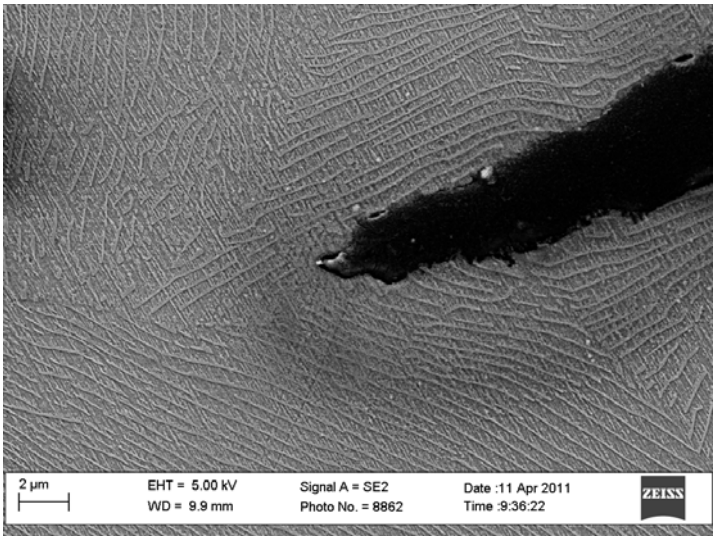

Figure 10. Microstructure showing pearlite lamellas (lines) surrounding a part of a graphite particle (black area).

Pearlite grows by simultaneous growth of ferrite and cementite grains from the grain boundaries into the austenite grain. The direction of each pearlitic domain is the same within one domain but the direction between different domains varies. Pearlite starts by nucleation of either cementite or ferrite at the grain boundaries. This nuclei has one semi coherent edge and one incoherent edge. This minimizes the activation energy barrier (see nucleation). The incoherent part grows faster because it has a higher mobility and for this reason they get the lamellar shape. The movement of the incoherent phase requires diffusion of carbon since the parent phase (austenite 0.76 wt% C) has different composition than the product phases (ferrite 0.022 wt % carbon and cementite with 6.7 wt % carbon). This means that C is diffusing to the cementite forming ferrite (carbon depleted zone). For this reason it can be concluded that the diffusion occur between the lamellas (18),(8).

2.9 Etching

The microstructure contains many different phases. For a sample that is polished it is impossible to tell the difference between the matrix phases (in an ordinary light microscope). This is why etching is important since etching makes it possible to tell the difference between the phases.

The etchant generally consists of a mixture of acids or bases with oxidizing or reducing agents. To explain what and how much it will affect the microstructure, Pourbaix diagrams (showing the oxidation/reduction potentials) is used. For iron and water system a Pourbaix diagram is shown in Figure 11.

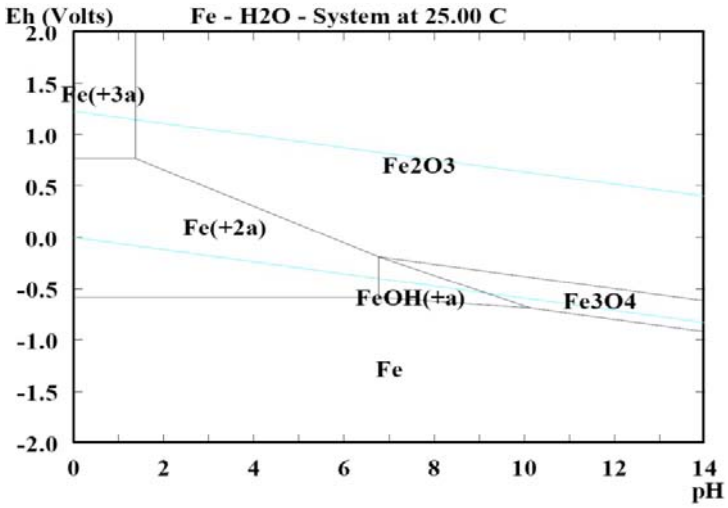

Figure 11. Pourbaix diagram showing an iron-water system. The pH change the possibility to oxidize iron.

For the iron diagram it can be seen that it oxidizes at lower pH but poorly at high pH. For this reason it is often etched with Nital which contains nitric acid which is an oxidizing acid,(20). It is important to notice that Pourbaix diagrams do not tell anything about the reaction speed.

3 Mechanical properties and mechanical testing of grey cast iron

---

CHAPTER INTRODUCTION

The aim of this chapter is to give basic knowledge in the most common tests and to discuss the mechanical properties of grey cast iron. What units, formulas, typical graphs and basic theory of the test methods for static, dynamic mechanical properties at room temperature and at increased temperatures. The latter to give a correlation to the higher temperature properties since this cannot be tested in this work.

3.1 Static mechanical properties

Small variations in chemical compositions even for the same material (different variations of grey cast irons) lead to different mechanical properties. They also differ depending on if the load is tensile, compressive or shear. The most commonly used tests to determine mechanical properties are the tensile and hardness test.

Tensile test

When performing a tensile test a stress-strain curve is achieved. From the curve a lot of mechanical data can be derived e.g. it is possible to determine how the material behaves elastically and plastically (permanent deformation). An illustration of a typical stress-strain curve is shown in Figure 12. Some of the different parameters that are possible to derive from the curve are;

E = Young's modulus	E describes the stiffness of the material.
UTS = Ultimate tensile strength	UTS is the maximum stress value that the material reaches before it breaks.
YS = Yield stress	This is the maximum stress that can be applied without giving rise to any permanent (plastic) deformation of the material.

The diagram uses the stress (σ) on one axis and the strain (ε) on the other. The stress is calculated by:

$$\sigma = \frac{F}{A_0} \qquad \textbf{Equation 6}$$

Where F is the force and A_0 is the area (of the unloaded specimen).

The strain (ε) is typically measured by an extensometer.

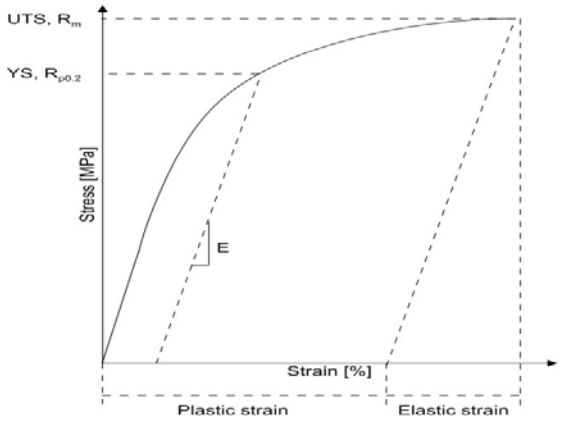

Figure 12. Illustration of a tensile test curve.

Gray cast iron has no clear yield point. As soon as the load is applied some parts of the material starts to deform plastically. For this reasons either tangent or secant modulus is used see Figure 13.

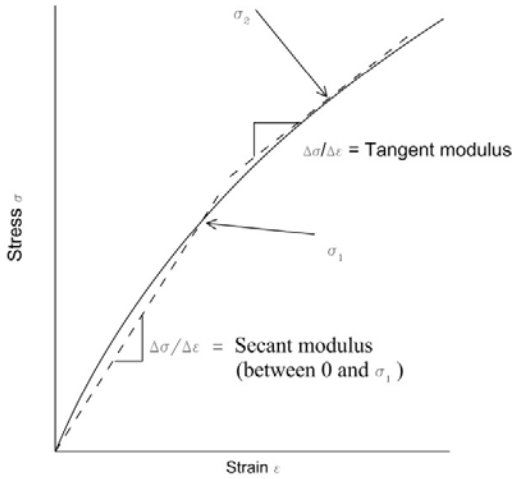

Figure 13. Stress-strain diagram showing non-linear elastic behavior.

Since the material is partly elastic and partly plastic during tensile loading the resulting curve from a tensile test can be seen as the total curve as shown in Figure 14.

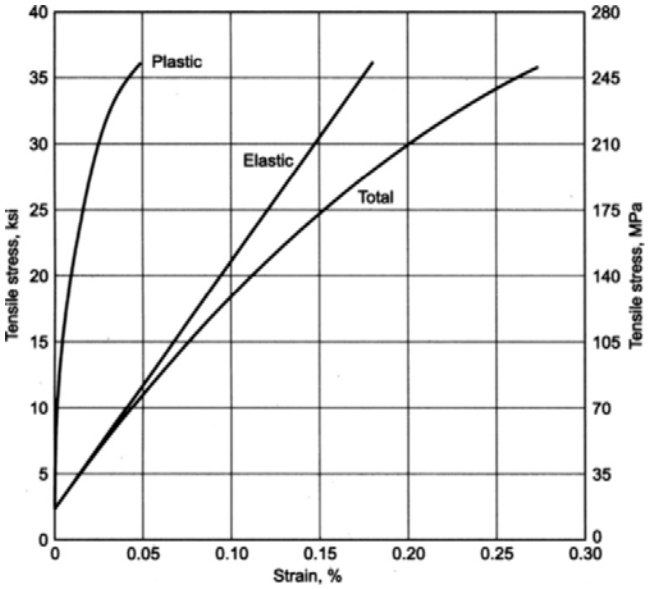

Figure 14. Total strain of a pearlitic grey cast iron (21).

Influence of microstructure on deformation behavior

Grey cast iron is a brittle material that deforms plastically to a large extent. When the load is applied, large stress concentrations will occur at the tip of the graphite flakes (18). This means that the strength is correlated to the microstructure and thus mainly to the appearance of graphite. To control the microstructure and strength, cooling rate and chemical composition are to be changed.

The graphite lamella contributions are affecting the mechanical properties the most. This makes the amount, size, morphology and distribution important factors. A higher graphite content (higher CE) and longer graphite flakes reduces the elastic modulus and decreases strength. This makes the modulus sensitive to alloying composition, making the modulus unique for each composition.

Another microstructural component that affects the mechanical properties is the size of the eutectic cells. A high amount of cells per volume means high tensile strength. So, by using inoculants smaller grains are formed while overheating and too much exposure time gives larger grains (19).

The pearlitic matrix contains two phases, ferrite and cementite. Ferrite is a high ductility and low strength phase and cementite is a hard and brittle intermetallic compound. The property of pearlite depends on the lamella spacing between the ferrite and cementite; smaller space increases the mechanical strength (19). The formation of pearlite is desirable in many processes and is therefore promoted by addition of certain alloying elements. Elements that promote pearlite are e.g. Cu and Cr (see Alloying element). Since Cu segregates in the last solidified region and Cr in the first they can be combined to give a homogeneous material for different component thickness. Details about the effect on mechanical properties when using Cu, Cr and N are described in Table 4.

Table 4. Effect on mechanical properties by additions of Cu, Cr and N.

Element	Effect	Cause
Cu	Increasing tensile strength up to 0.35% Cu.	Cu leads to forming of more pearlite which leads to higher strength. Above 0.35% it is thought to be fully pearlitic. If the carbon level is decreased shorter graphite is formed which also give rise to higher strength.
Cr	Increasing strength in all section sizes with increasing amount Cr. Shorter and thinner graphite flakes. Easier to achieve a homogeneous material with even hardness trough thickness.	One theory is that Cr combines with carbon and reduces free carbon, which leads to decreasing pearlite lamella spacing. This results in increasing matrix homogeneity, hardness and strength.
N	Increases strength and changes roundness of graphite	Promotes pearlite, but in large concentrations it forms gas bubbles that form pinholes.

Hardness

Hardness is a measure of the materials resistance to plastic deformation and hardness and strength are often strongly correlated. With an increased hardness the strength also increases. For this reason the discussion about tensile strength and dynamic mechanical properties holds for hardness as well.

3.2 The effect of graphite particles in grey cast iron described by Fracture mechanics

Grey cast iron contains graphite particles and as mentioned before these can be thought of as cracks. Therefore it is important to understand how cracks affect the material. This is partly described by fracture mechanics theory. To be able to quantify the effects of flaws in materials Griffith's crack theory is needed.

Griffith assumed that the lower fracture strength is due to microscopic flaws in the bulk material. To test this, a crack (large flaw) was induced to the surface. Tests led to the expression:

$$\sigma_f \sqrt{a} \approx C \qquad \textbf{Equation 7}$$

where a is the crack length and σ_f the stress at fracture.

This predicts that the stress (and also the strain) for a linear elastic material at the crack tip is infinite. This is not solvable and therefore demands another approach. Griffith solved this by using thermodynamics. When a crack forms it creates two new surfaces which mean that the surface energy increases and at the same time the potential energy changes. The potential energy is calculated as the area under the stress strain curve in the elastic region, $\int_0^{\varepsilon_y} \sigma * d\varepsilon * Geometric\ factor$.

Thus, by determining the relationship between the decrease in potential energy and the increase in surface energy a model of fracture mechanics can be derived. To get a good model for this the following steps are performed:

- **Configuration, see Figure 15 .**

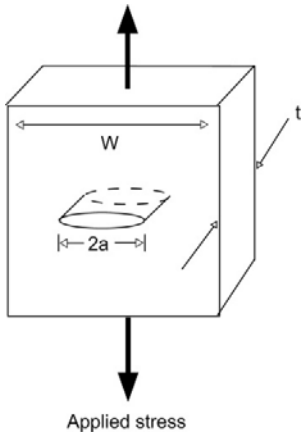

Figure 15. Crack in a large plate.

- **Assumptions and original form:**
  The total crack surface area is $\mathbf{2a * 2 * t}$ and the specific surface energy is $\boldsymbol{\gamma_s}$ (energy/unit area). The specific surface energy is raised when an atom has less neighbor connected to it, i.e. surface atoms has higher free energy than the ones in the matrix. By using stress analysis it is possible to compute the decrease in potential energy of the infinitely large cracked plate as $\frac{(\boldsymbol{\pi\sigma^2 a^2 t})}{\boldsymbol{E}}$.
  The equation for the change in potential energy can then be written:

$$U - U_0 = -\frac{(\pi\sigma^2 a^2 t)}{E} + 4at\gamma_s \qquad \textbf{Equation 8}$$

Where U =potential energy of body with crack
U_0 = potential energy of body without crack
t = thickness
σ = applied stress
a = one half crack length, t= thickness
E = modulus of elasticity
$\boldsymbol{\gamma_s}$ = specific surface energy

- **Equilibrium:**
  Equilibrium is calculated by differentiating the potential energy with respect to crack length and set this to zero. Since U_0 does not vary with length it is zero, which gives the equation:

$$2\gamma_s = \frac{2\pi\sigma^2 a}{E} \qquad \textbf{Equation 9}$$

- **Final equation:**
  Equation 9 is rewritten into:

$$\sigma = \sqrt{\frac{2E\gamma_s}{\pi a}} \qquad \textbf{Equation 10}$$

This can be used to give a hint on what stress levels that are possible to attain before the cracks begin to propagate (only accurate for brittle materials).

When tensile test are performed on grey cast iron the graphite will act as cracks due to the low tensile strength of the graphite phase. Since grey cast iron has no distinct elastic zone it is harder to determine the potential energy. The graphite appearance varies a lot for the different materials and for that reason the expected stress levels will vary. Since the theory describes cracks in terms of a single crack it can be used very locally and as a principle in the reasoning of the stresses that occur on a microstructural level, around and within the eutectic cells.

3.3 Dynamic mechanical properties

The main use of grey iron is in engine components. Since all engines are exposed to cyclic stress (the nature of an engine), there is always a risk of fatigue. For this reason it is important to be aware of the dynamic mechanical properties of the material.

Dynamic properties are tested by cyclic loading. The common tests are tension-compression, bending and twisting. From these tests it can be concluded that the matrix hardness and decreasing graphite size are parameters that improves the fatigue properties (22).

Crack propagation occurs when grey iron is exposed to cyclic tensile stresses. Since graphite has very low strength these serve as a natural path for a crack to grow since the crack most likely follows the path of lowest fracture energy. The main contribution to the strength is in the areas between the eutectic cells where much energy is absorbed. Cracks can propagate trough the eutectic cells. In the eutectic cells there exist small areas of matrix between the graphite (matrix bridges). But since these areas are very small inside the eutectic cells their contribution to the overall toughness is small (23).

One reason why the fatigue strength of grey iron is affected by eutectic cells is because the graphite in the eutectic cell is not crossing the boundary between the cells. For this reason one of the main contributors to the absorbed energy during fracture is the boundary region (23).

Thermo mechanical fatigue (TMF)

Grey cast iron is known for its good thermo mechanical fatigue resistance. It is known that materials with high rupture stress and high heat conductivity provide high resistance to thermal fatigue. Other factors that determine thermal fatigue are elastic modulus and thermal expansion. The thermal stress from the factors can be described by:

$$\sigma = \alpha_l E \Delta T \qquad \textbf{Equation 11}$$

Where σ = Thermal stress
α_l = Thermal expansion
E = Modulus of elasticity
ΔT = Temperature change

Since the data for the same parameter differs a lot between different sources it is hard to tell exact relationships. For grey cast iron it can be concluded that the graphite affects the thermal properties to a great extent (24).

Fatigue of grey cast iron vs. eutectic cell size

As mentioned above, a high amount of eutectic cells (many small) give a high strength. Since tensile strength can be correlated to endurance limit, i.e. the stress level below which it can be exposed to unlimited cycles, this gives a hint regarding the fatigue properties.

Baker (25) observed a decrease in ultimate tensile strength with increasing eutectic cell size (Figure 16). Figure 16 is valid for a compacted graphite iron and the result for a gray cast iron may differ. It can be seen that there is an optimum cell size if both fatigue and strength is taken into account.

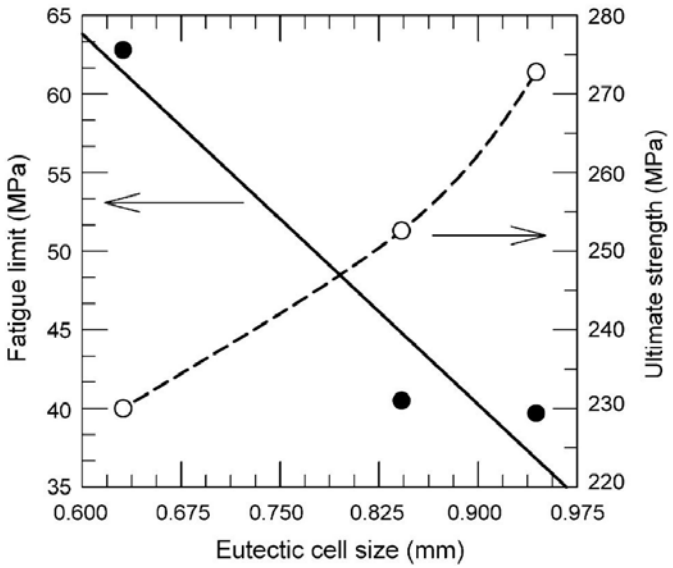

Figure 16. Effect of mean size of eutectic cells on fatigue (dashed line) and ultimate strength (solid line) for a compacted graphite iron.

4 Statistics and data analysis

CHAPTER INTRODUCTION

This chapter is intended to give the basic background to linear regression and how it can be used to correlate different parameters. For example it can reveal if there is any correlation between Cu, Cr and N content and strength. It describes the principles mathematically but tries to connect them with the project data.

The aim of linear regression is to model a relationship between a scalar variable and one or more variables. The unknown parameters are estimated from the data using linear functions.

4.1 Fitting of data

It is assumed that there is a linear dependence between the variables X and Y, where X is known. This forms an ordinary linear equation:

$$Y = \beta_0 + \beta_1 X \qquad \textbf{Equation 12}$$

When Y values and errors are observed, Equation 12 is rewritten into:

$$Y = \beta_0 + \beta_1 X_1 + \beta_n X_n + \varepsilon \qquad \textbf{Equation 13}$$

In this equation ε is a stochastic variable and Y is called the dependent variable. In statistics the dependent variable is the event that is expected to change when the independent variable is altered (26).

Fitting the data is done by using a common method called linear least squares. It minimizes the total distance of the data scatter to the calculated line see Figure 17.

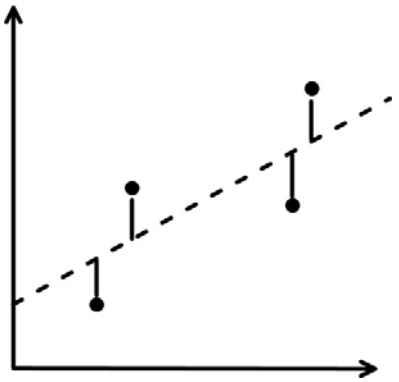

Figure 17. Distance for the data to the fitted line.

The least squares condition is stated as:

$$R^2 = \sum_{1}^{n} [y_n - f(x_n, \beta_1, \ldots, \beta_n)]^2 \qquad \textbf{Equation 14}$$

In Equation 14, y_n are the dependent variables, x_n, the independent, β the sought parameter, f the linear fit and R^2 the quadratic error. This equation only shows the deviation of the data from the fit. To be able to make the deviation as small as possible (fit the data) it is differentiated with respect to each parameter and

sat to zero: only shows the deviation of the data from the fit. To be able to make the deviation as small as possible it is derived with respect to each parameter and sat to zero:

$$\frac{\partial(R^2)}{\partial\beta_n} = 0 \qquad \textbf{Equation 15}$$

By differentiating Equation 14 for each parameter it forms an equation system. When there are more than one parameter the matrix notation is more convenient. For this reason the equation system is written as:

$$Y = X\beta \rightarrow \begin{bmatrix} Y1 \\ Y2 \\ Y3 \end{bmatrix} = \begin{bmatrix} 1 & X_{1Cu} & X_{1Cr} \\ 1 & X_{2Cu} & X_{2Cr} \\ 1 & X_{3Cu} & X_{3Cr} \end{bmatrix} \begin{bmatrix} \beta_0 \\ \beta_1 \\ \beta_2 \end{bmatrix} \qquad \textbf{Equation 16}$$

(In Equation 16 Cu and Cr are used as indexes to show how it can be applied to the tests for gray cast iron).

The solution to Equation 16 is given by:

$$X^TY = X^TX\beta \rightarrow \hat{\beta} = (X^TX)^{-1}X^TY \qquad \textbf{Equation 17}$$

The transpose matrices are there to fit the size of the matrices, which is needed to solve the system.

Now the parameters are known and it is possible to calculate the stochastic variable by using Equation 13:

$$\varepsilon = Y - X\hat{\beta} \qquad \textbf{Equation 18}$$

Here $X\hat{\beta}$ is the fitted value and ε the deviation from Y (ε is often called the disturbance).

4.2 Analyze of fitted data

The most important graph to make is the residual plot. It is a plot consisting of ε and Y. This plot gives information about the plausibility of the model (27).

If the model is considered valid it is possible to calculate variance for the residuals. By doing that it is possible to calculate the uncertainty of the calculated coefficients (e.g. β_0 and β_1) and the uncertainty for the regression line. (Other parameters can be calculated but these are just examples that are used in the work).The variance for the parameters is calculated as:

$$Var[\hat{\beta}] = \sigma^2(X^TX)^{-1} = \sigma^2 \begin{bmatrix} C_{11} & C_{12} \\ C_{21} & C_{22} \end{bmatrix} \qquad \textbf{Equation 19}$$

The X in this equation is the matrix X used before, called the design matrix. In this example two parameters are used. From this it is possible to get the variance for each parameter:

$$Var[\widehat{\beta_0}] = \widehat{\sigma^2}C_{11} \text{ and } Var[\widehat{\beta_1}] = \widehat{\sigma^2}C_{22} \qquad \textbf{Equation 20}$$

The confidence interval can now be calculated with the assumption that ε is normally distributed around zero. First the variance of the residuals is calculated as:

$$\widehat{\sigma^2} = \frac{Y^TY - \hat{\beta}^TX^TY}{n-p} \qquad \textbf{Equation 21}$$

In this equation p is the number of parameters. The numerator is the sum of squares for the residuals.

From this it is possible to formulate a t-distribution:

$$T = \frac{\hat{\beta}_j - \beta_j}{\hat{\sigma}\sqrt{C_{jj}}} \sim t_{n-p} \qquad \textbf{Equation 22}$$

And from Equation 22 it is possible to calculate the confidence interval as:

$$\beta_j = \hat{\beta}_j \pm t_{\alpha/2}\hat{\sigma}\sqrt{C_{jj}} \qquad \textbf{Equation 23}$$

The parameter is valid if the interval does not cross zero. If it crosses zero it is not possible to say that the parameter does not depend on chance.

5 Digital image correlation – Non contact deformation technique

CHAPTER INTRODUCTION

This chapter is intended to give the basic background to digital image correlation (DIC) theory. It describes the difference between 2D and 3D DIC. The main focus will be on 2D since it is used in this work.

Digital image correlation techniques (DIC) have become more widely used with the increased performance of computers and digital images. DIC uses pattern sprayed on the material or if the material has a good contrast in the microstructure it uses it as the pattern. With the first image as a reference it then determines the local differences (local strains) in the subsequent images. The differences give rise to a correlation coefficient, which describes the amount of difference i.e. it identifies the changes in pattern by taking the pattern with the highest correlation. There are two modes possible, two-dimensional (2D) and three-dimensional (3D) (28). The 2D mode uses one camera and acquires images of a flat surface while the 3D mode uses two cameras from which images a 3D image of bent surfaces is derived.

The methods use difference in grayscale when operating. These differences may be easy to see and explain, but are hard to mathematically describe. This demands advanced algorithms (28).

5.1 2D-DIC

As mentioned above the2D analyze uses one camera. This camera is directed perpendicular to the test surface, which is put into a tensile machine and a load is applied. The deformation of the material occurs in-plane and therefore it is important that no out-of-plane motions occur which might be interpreted as pseudo image deformation by the software. From the deformation it is possible to read three different strain fields, ε_{xx}, ε_{yy} and the shear strain ε_{xy}.

To achieve good testing conditions three points needs to be fulfilled:

- The test piece should have a flat surface.
- The surface should be at the right distance and angle to the objective/camera.
- Out-of-plane movement should be minimized by correct setup.

For the last two points it is important to notice that vibrations affect the image quality and that the vibrations can come both from the tensile testing machine and the camera frame (28).

6 Experimental methods

CHAPTER INTRODUCTION

This chapter aim to describe how things were done, what equipment was used and how some problems were avoided by using other methods than the initial ideas.

6.1 Experimental materials

Scania made a full factorial experimental design from which seven materials were taken and investigated in this thesis work. Their chemical composition is summarized in Table 5.

Table 5. Chemical composition of the materials.

Melt	Flask	Plate	C	Si	Mn	S	P	Cr	Ni	Mo	Cu	Ti	Al	Sn	N	CE
			wt-%	wt-%	wt-%	wt-%	wt-%	wt-%	wt-%	wt-%	wt-%	wt-%	wt-%	wt-%	ppm	wt-%
1	**2**	2A	3.67	1.72	0.54	0.059	0.027	0.078	<0.050	0.013	0.51	0.006	0.001	0.005	70	4.12
1	**7**	2A	3.56	1.74	0.56	0.058	0.028	0.161	<0.050	0.012	0.62	0.006	0.001	0.000	80	4.00
1	**11**	2A	2.76	1.74	0.59	0.063	0.026	0.063	0.057	0.014	0.33	0.005	0.003	0.008	85	3.21
2	**2**	2A	3.41	1.98	0.71	0.07	0.033	0.31	<0.050	0.014	0.50	<0.010	0.002	<0.010	90	3.92
2	**3**	2A	3.36	2.00	0.70	0.66	0.031	0.36	<0.050	0.014	0.50	<0.010	0.002	<0.010	90	3.88
2	**4**	2A	3.41	2.04	0.70	0.068	0.031	0.38	<0.050	0.012	0.52	<0.010	0.002	<0.010	110	3.93
2	**6**	2A	3.36	2.00	0.70	0.068	0.033	0.35	<0.050	0.014	0.50	<0.010	0.002	<0.010	150	3.87

From the table it can be seen that melt 1 has no N, while melt 2 has different levels of N. It can also be seen that melt 2 is stable in its Cu and Cr levels, while melt 1 varies.

6.2 Microstructure analysis

To gather data regarding the microstructure, a cutting machine, cold mount material, a polishing machine, chemicals, a light microscope, an automated table and image analysis software were used.

Small samples were cut from test bars and cold mounted. Three series with seven samples each were made. Two series with small samples in different directions and one with the entire test bar see Figure 18 .
Serie 1 was cut out (horizontally) and ground vertically, serie 2 was cut out and ground vertically and serie 3 was ground directly.

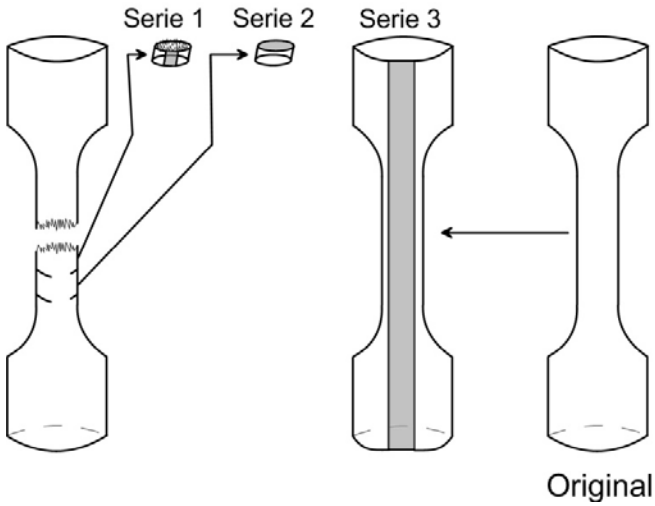

Figure 18. Test series and their prepared surfaces (shown in grey).

For the large piece (serie 3), 0.2 mm was milled away and a surface approximately 2 mm wide was made. This piece was used for digital image correlation analysis at tensile testing. All series surfaces were prepared according to Table 6**.**

Table 6. Preparation steps of test samples.

Activity	Equipment	Time
Grinding	SiC-paper 220	60 s
	SiC-paper 320	60 s
	SiC-paper 500	60 s
	SiC-paper 1000	60 s
Cleaning	Cotton and ethanol	~ 4 s
Polishing	MD-DUR 9µm diamond paste	7 min
	MD-MOL 3µm diamond paste	5 min
	MD-NAP 1µm diamond paste	2 min

Many images were put together to a large picture, by a method called mosaic. Each image was taken at a magnification of 100x and at a resolution of 1360x1024.The order of the taken images is shown in Table 7.1. The optics of the microscope changed the orientation which led to an orientation rotation of 180 degrees forming a new matrix see Table 7.2.

Table 7. Showing images as taken and as software puts it together.

As seen on sample (4.1)		
1	8	9
2	7	10
3	6	11
4	5	12

As put together by software (4.2)		
12	5	4
11	6	3
10	7	2
9	8	1

From calibration data (see
Table 8) the pixel to length ratio is shown, which made calculations of the total surface possible. It was calculated to 17.26mm^2 see Table 9. This large image surface area allows more accurate data.

Table 8. Calibration data.

Magnification	Direction	Resolution	Pixel	Length(µm/pixel)
100x	X	1360	1	1.02041
	Y	1024	1	1.01215

Table 9. Calculation of total sample area.

Direction	Calculation of total length (Image*Resolution*Length)	Total length (µm)	Total Area (mm^2)
X	3*1360*1.02041	4163.27	17.26
Y	4*1024*1.01215	4145.77	

To analyze the graphite amount, the graphite morphology, presence of ferrite, eutectic cell size and eutectic cell morphology different macros for the software Leica Qwin V3 were used. They were all analyzed at the same surface size but after different etching methods see Table 10.

Table 10. Etchant effect on samples.

Etchant	Domains/phases that are exaggerated in the microstructure
None	Graphite
Nital 3%	Ferrite and pearlite
Alkaline sodium picrate	Eutectic cells

Alkaline sodium picrate is the etchant that forms the colored microstructure. The etchant consist of 100 ml of a 2 vol% (saturated aqueous solution) picric acid with 25g sodium hydroxide under constant stirring. At mixing an exothermic reaction takes place and the temperature will increase to 60-70^{o}C. After the temperature is reached, additional energy is put to the solution by heating until it reaches 80^{o}C. The cast iron materials were then put into this solution for times between 20 – 30 minutes.

To make a 3 % nital solution, 3 ml 65 vol% nitric acid is mixed with 100 ml ethanol.

Three macros were used for the analysis; one for graphite amount, another for the graphite morphology and a third for the eutectic cells. None were used for analyzing ferrite, since that analyze was made by ocular inspection after etching the surface with Nital. In this study the total matrix composition is described as: 100% = %Pearlite + %Ferrite + %Graphite.

6.3 Tensile testing

Tensile tests were carried out with a Sintech 20/D tensile machine with the software Inersjö. It was run according to standard ISO 6892-1.The strain rate was set to 0.3 mm/min and deformation was measured by an extensometer with a gauge length of 50 mm. To prevent damage to the extensometer it was removed at 0.6 % elongation. The more accurate data from the extensometer was used to calculate the tangent modulus ($E_{0.2}$). It was set to be measured at 0.2 % elongation per definition.

The used test bar was a standard test bar (10C50) with a diameter of 10 mm, a threaded M16 head and a length of 70 mm according to standard ISO 6892-1. To get a flat surface along the specimen for the DIC-analysis milling was used. The flat surface was ground, polished and etched to reveal a desired microstructure as shown in Figure 19.The test bars were held by spherical bearings in the tensile test machine.

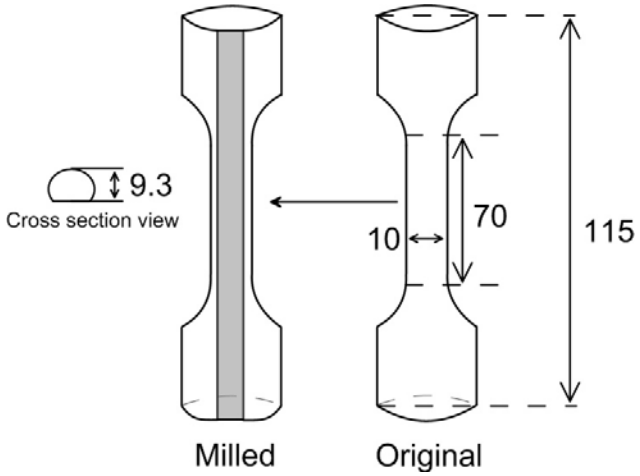

Figure 19. Test bar according to standard versus a milled test bar.

Since some part of the area was cut away at milling a new diameter needed to be calculated. This was calculated by subtract the original area with the milled area, which gave the new total area. This new area was assumed circular to be able to get a new diameter. The tensile machine was programmed to run load cycles according to Figure 20.

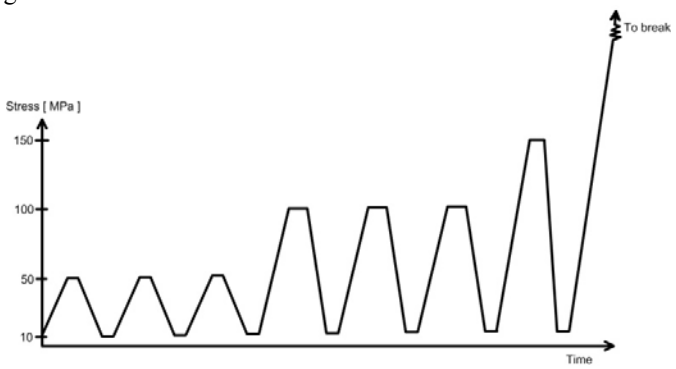

Figure 20. Cyclic load scheme.

To skip the first out of plane noise that occurs when the test bar is fixating into its position a pre-stress of 10 MPa was used. Each cycle starts and stops at this level for the same reason.

6.4 Digital image correlation

In section 6.4.1 Aramis is referred to in the text, but it is described in the next subchapter (6.4.2).

6.4.1 Camera and microscope

The camera used to the Aramis system was a CCD-4000G with a resolution of 4 Megapixel. It was mounted on a microscope with an MPlan Apo objective with a magnification of 2 times and a working distance of 34 mm as shown in Figure 21. The total magnification was 20 times. During the tensile test the image sample rate was 12 images/min. The photographed area was approximately 8.5x8.5 mm^2 and the camera resolution was 2048 x 2048 pixels which results in approximately 4.15 µm/pixel.

Figure 21. Camera mounted on a microscope capturing sample surface.

When the tensile test machine starts the upper part moved and the lower part was stationary. The loading direction can be seen in Figure 22. The optics rotates the images by 180 degrees so that they are showed upside down on the computer screen.

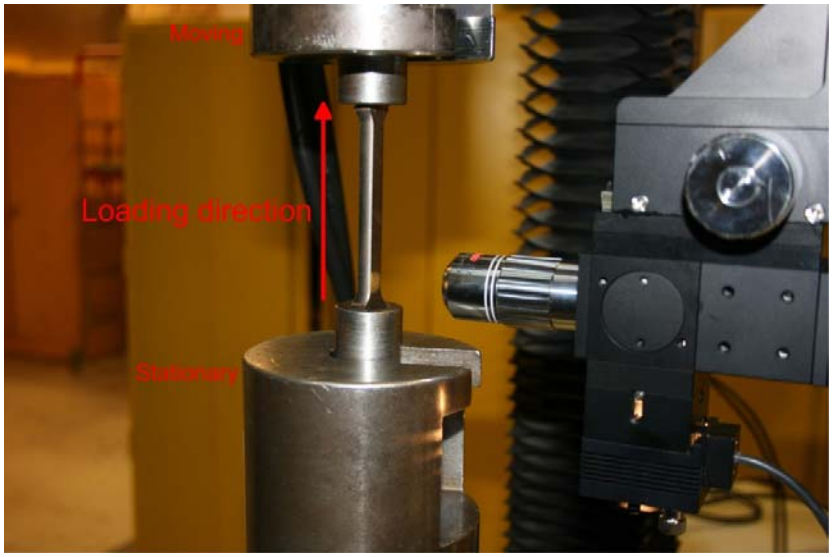

Figure 22. Loading direction of the test bar.

6.4.2 Software

The digital image correlation software used was Aramis. The software analyses the acquired images by dividing each image (called stage by the software) into facets. By using correlation techniques based on the specific appearance of these facets it is possible for the program to calculate the displacements and strain-fields. The standard facet size is 15 x 15 pixels with a 2 pixel overlap. In some cases more accurate facets must be set to be able to calculate the deformation, at the expense of speed, and special resolution. As a rule of thumb each facet should contain at least thirty gray scales to identify a pattern. This is important for the strain computation and visualization. In the experiments of this thesis work different facet sizes and overlaps were tested. The final facet size used was 50 x 50 pixels with a 2 pixel overlap, which gave a high strain resolution.

To start the calculations a starting point has to be selected. This starting point should be at a point of good focus, have a distinct difference in grayscale and should not move out of the field of view during deformation. The starting point is thus a facet that is referred to in all stages.

In this work Aramis is identifying a natural pattern. This pattern is a black and white image of the color etched samples. During tensile tests one camera was used which means that it measures in 2D. The resulting images were masked to save computation time and increase accuracy. Aramis used linear strain to calculate the local strains. This means taking measuring points derived directly from the facets. Another method possible is spline strain computation which uses interpolated points in the calculations.

6.5 Data analysis

The data was analyzed according to chapter 4. Based on the least squares method all data was tested by the multivariable regression analysis and looked for dependencies and significance. The multivariable software used for the calculations was written in Matlab.

7 Results and discussion

CHAPTER INTRODUCTION

This chapter aims to present the actual results and limitations. The discussion starts with the color etched microstructures and the corresponding chemical data to give a description of the different materials and their mechanical properties. This is thought to give the reader an illustrative explanation and connection to the result.

All chemical results are given in weight percent as standard. The design of experiments is done by a software called Moddes and the results in table 11-13 were produced by Scania. The way Scania selected these compositions was by using a full factorial experimental design. Since it is hard to get exact compositions from the foundry they use a multivariate data analysis.

7.1 The effect on microstructure with different chemical compositions

The effect of the different chemical compositions can be seen in the color etched microstructures. The chemical data are shown in Tables 11-13 and their corresponding microstructural images in Figures 23-25.

Table 11. Chemical compositions for materials 1.2.2A, 1.7.2A and 1.11.2A.

Material	Cu (wt %)	Cr (wt %)	N (ppm)	CE*	Inoculant (wt %)
1.2.2A	0.51	0.078	70	4.12	0.2
1.7.2A	0.62	0.161	80	4.00	0.2
1.11.2A	0.33	0.063	85	3.21	0.2

* CE is calculated as Equation 1.

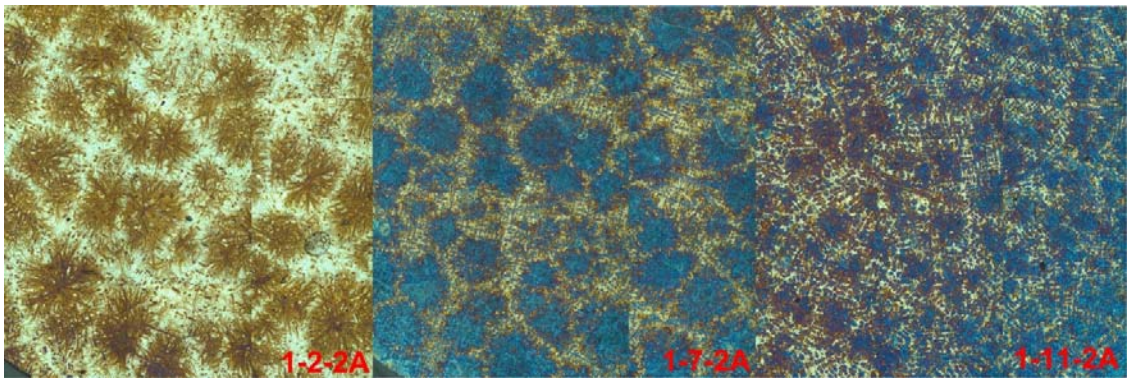

Figure 23.Color etched mosaic images for material 1-2-2A, 1-7-2A and 1-11-2A. The images show different size, amount and distribution of cells. All images are approximate squares with the sides close to 4.16 mm and are taken at 100x magnification.

The different color appearances are due to the individual etching properties of the materials. The etching time for the different materials was about the same for all samples. The used etching agent called alkaline sodium picrate is developed to show eutectic cells and primary austenite which can be seen on all images. The largest chemical difference for the materials in Figure 23 is the CE composition. This affects the amount of primary austenite and the size of the graphite particles.

Table 12. Chemical compositions for materials 2.2.2A, 2.3.2A and 2.4.2A.

Material	Cu (wt %)	Cr (wt %)	N (ppm)	CE*	Inoculant (wt %)
2.2.2A	0.50	0.31	90	3.92	0.0
2.3.2A	0.50	0.36	90	3.88	0.2
2.4.2A	0.52	0.38	90	3.93	0.4

* CE is calculated as Equation 1.

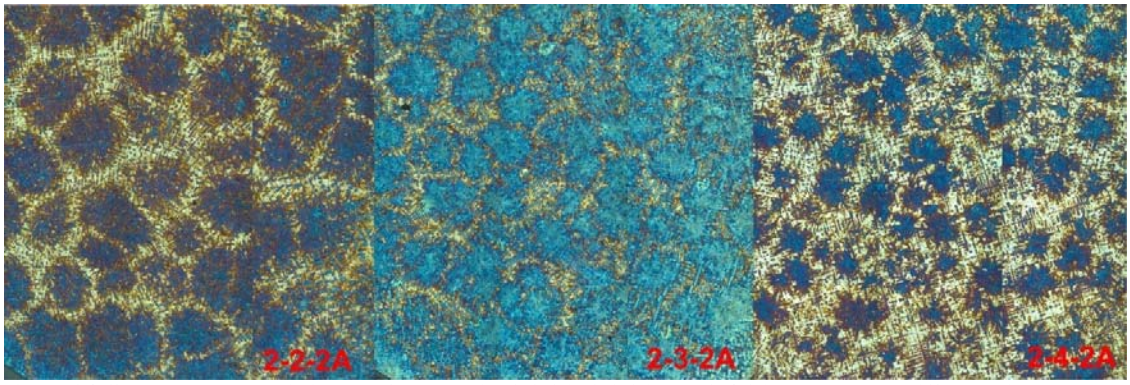

Figure 24.Color etched mosaic images for material 2-2-2A, 2-3-2A and 2-4-2A. They show different size, amount and distribution of cells. All images are approximate squares with the sides close to 4.16 mm and are taken at 100x magnification.

Figure 24 show materials with different inoculants while the rest of the chemical compositions are similar for the three materials. The difference in cell size and border width is notable.

Table 13. Chemical composition for material 2.6.2A.

Material	Cu (wt %)	Cr (wt %)	N (ppm)	CE*	Inoculant (wt %)
2.6.2A	0.50	0.35	150.00	3.87	0.20

* CE is calculated as Equation 1.

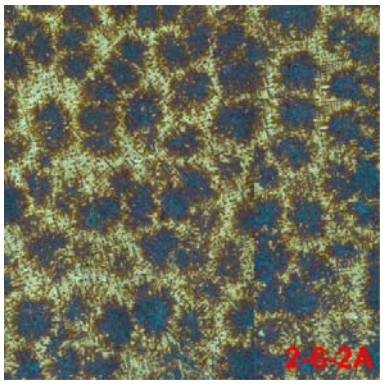

Figure 25. Color etched mosaic images for the material 2.6.2A. The image sides are 4.16 mm and are taken at 100x magnification.

Material 2.6.2A has higher amount of N than the rest of cast 2. This affects the roundness of the graphite particles. The inoculant amount is the same as for 2.3.2A and for that reason their cell size should be close to each other which can be observed by comparing figure 24 and 25.

7.1.1 Change in microstructural particles and phases

The different chemical composition affects the microstructures at different stages of the casting process. Some of these changes are discussed for graphite, pearlite and cementite in the following parts.

Graphite

The graphite size and distribution is easier to see on an unetched surface. The different forms of graphite in the different samples are shown and summarized in Table 14. These values are judgments made according to the distributions given in Figure 5.

Table 14. Type of graphite for the different materials.

Material	1.2.2A	1.7.2A	1.11.2A	2.2.2A	2.3.2A	2.4.2A	2.6.2A
Type	A, B	B	C, E	A, D	A, C	A, B	A, D

For the same type, the graphite showed different appearance in terms of length, area and particles/area which is shown in Table 15.

Table 15. Mean values of area, length and particles/mm^2. These are calculated with a software called Leica QWin using the mosaic images with a surface of 17.2mm^2. This data is log normal distributed and are thereby calculated in log scale to get the correct mean values.

Material	1.2.2A	1.7.2A	1.11.2A	2.2.2A	2.3.2A	2.4.2A	2.6.2A
Length [µm]	48	55	43	51	51	53	47
Area [µm^2]	162	272	198	216	245	254	204
Particles/mm^2	205	165	146	165	161	155	172

Material 1.11.2A had the lowest CE which could explain the small graphite flakes that occur mainly as E type. Material 2.2.2-2.4.2A has fixed values for all elements except from inoculants see table 11-13. Sample 2.2.2A has the lowest content of inoculants while 2.4.2A has the highest. For this reason 2.4.2A requires less undercooling and should promote graphite of type A.

For the rest of the material it is hard to tell what alloying element that affects graphite in what way since they are all varied at the same time.

Pearlite

All materials were etched with 3% nital to reveal ferrite. Only material 1.2.2A showed small fractions of ferrite (<1%). The other material matrixes were considered fully pearlitic. The optical resolution on the light microscope was too low to determine the spacing of the lamellas. No distinction between the materials pearlite structure was done.

Cementite

Besides the cementite found in pearlite, cementite was not further investigated.

7.1.2 Macrostructural changes

The lack of samples from all of the original full factorial designed experiment made the study of the experimental design incomplete and for that reason it was hard to distinguish between the effects of the different chemical compositions. Therefore the focus will be on changes in properties and structure due to changes in addition of inoculants.

Eutectic cell size and morphology

From the color etched Figures 23-25 it can be seen that the size and distribution of the eutectic cells varies.

Table 16. Cell data for all materials studied. The cell diameter is an average value of the collected data from the Leica QWin software and the mean cell space value is measured as the mean between the centers of the cells.

Material	1.2.2A	1.7.2A	1.11.2A	2.2.2A	2.3.2A	2.4.2A	2.6.2A
Cell area (μm^2)	$8.78*10^5$	$6.74*10^5$	$2.74*10^5$	$9.69*10^5$	$5.29*10^5$	$3.78*10^5$	$4.10*10^5$
Cell Diameter (µm)	990	902	650	1086	761	679	662
Cell space (mm)	1.236	1.032	0.844	1.140	0.924	0.840	0.768

There are not enough data to say with certainty that there is a correlation between cell area and cell diameter, but there is a clear trend as shown in Figure 26. The trend can be explained by the fact that the cells are close to spherical and for that reason the diameter and the area should have a correlation close to the area of a circle.
It can also be seen that both parameters are correlated to the amount of inoculant. This is supported by the literature; the more inoculants added the more nucleation sites for the cells to grow. For this reasons more and smaller cells are formed with more inoculants.

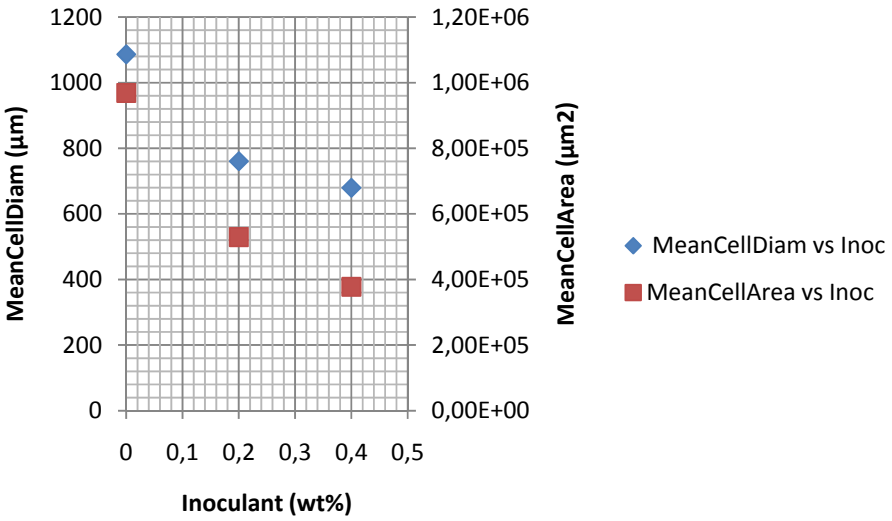

Figure 26. Change in eutectic cell diameter and area versus the amount of inoculant added.

The morphology of the cells can also be described by the distance between the centers of the cells. In Figure 27 the cell distance versus inoculant amount is shown.

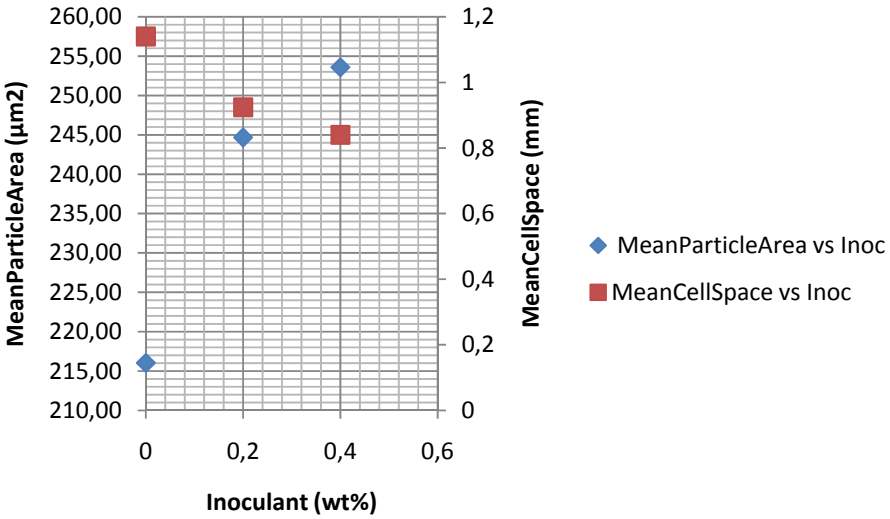

Figure 27. Mean particle area and cell distance versus the amount of inoculant added.

From the graph it can be seen that the space between the cells are decreasing with increasing amount of inoculant. This is explained by the same discussion as above: The more inoculant the more cells, the more cells the less distance between two cell centres. This makes extra sense by looking at Figure 24 where the increase in eutectic cell size can be seen.
The graph also shows the increase in particle area with increasing amount of inoculant. This may be explained by the fact that for graphite to grow large it demands longer cooling times or lower undercooling. In this case the lower demand of undercooling will be the probable cause.

Primary austenite

From Figures 23-25 different amount of primary austenite can be seen. This can be explained by the different content of alloying elements.
The difference in CE is affecting the materials austenite content the most. Different levels of CE for the materials can be seen in Tables 11-13 and the phase diagram in Figure 2.

Material 1.2.2A has the highest CE (4.12 wt%) and is thus close to eutectic composition. This mean that the austenite interval is small and less primary austenite is formed. This fact is strengthened by the microstructures presented in Figure 23 where less austenite is shown.

The other materials are harder to distinguish. They have lower and narrower CE-values. The appearance of the primary austenite depend on the liquids local temperature gradients which in turn depend on the composition in front of the solidification. This is explained by Figure 7. Since all the materials studied have different chemical compositions they all have different compositions ahead of the solidification. For that reason they all have different equilibrium temperature which means they have different demands of undercooling. From the color etched images it is possible to say that there are differences but it is hard to say what image belong to what composition just by looking at these structures.

7.2 Effect of microstructure on mechanical properties

From the "cyclic" tensile tests it was possible to collect data for the use in a regression model.

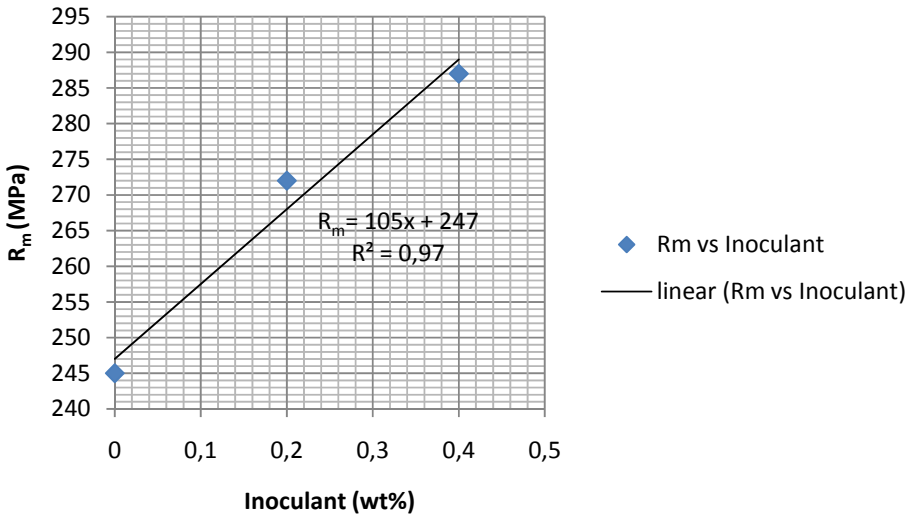

Figure 28. Amount of inoculant added versus R_m. The formula for the fitted line is: R_m= 105*Inoculant + 247, where the parameters are β_0 = 247 and β_1 = 105.

The validity of this method was tested by the R^2 value and by testing the parameters significance for a 95% confidence interval. The R^2 value is close to one which indicates a good fit, but the parameters confidence interval was:

β_0 = [190.1761 303.8239]
β_1 = [-115.0779 325.0779]

Since parameter β_1 crosses zero in its interval it cannot be significant. It is difficult to draw any conclusions from the small amount of data. (The number of parameters is close to the amount of data).
But the trend giving that, an increasing amount of inoculant added to the melt increases the strength, seems clear and is supported by the literature and is for these reasons accepted.

For all other alloying elements with the given data it is impossible to tell anything with certainty, since an isolation of any alloying element cannot be made (except for the inoculant).

The mechanical data for all the materials are summarized in Table 17.

Table 17. Mechanical data.

Material	1.2.2A	1.7.2A	1.11.2A	2.2.2A	2.3.2A	2.4.2A	2.6.2A
R_m (Scania) [MPa]	130	201	342	246	273	282	293
R_m (SP) [MPa]	103	163	213	181	214	227	236
R_m (SP.Cyclic) [MPa]	135	205	254	200	244	242	255
Tangent modulus [GPa]	48	89	137	101	108	103	114

The large increase in tangent modulus from sample 1.2.2A – 1.11.2A is due to the decrease in CE.

In previous part of chapter 7 and in the paragraph above, it was shown that inoculants change the appearance of the eutectic cells and that the amount of inoculant changed the tensile strength of the materials. For clarity the next graph show the same correlation for the cells versus mechanical properties.

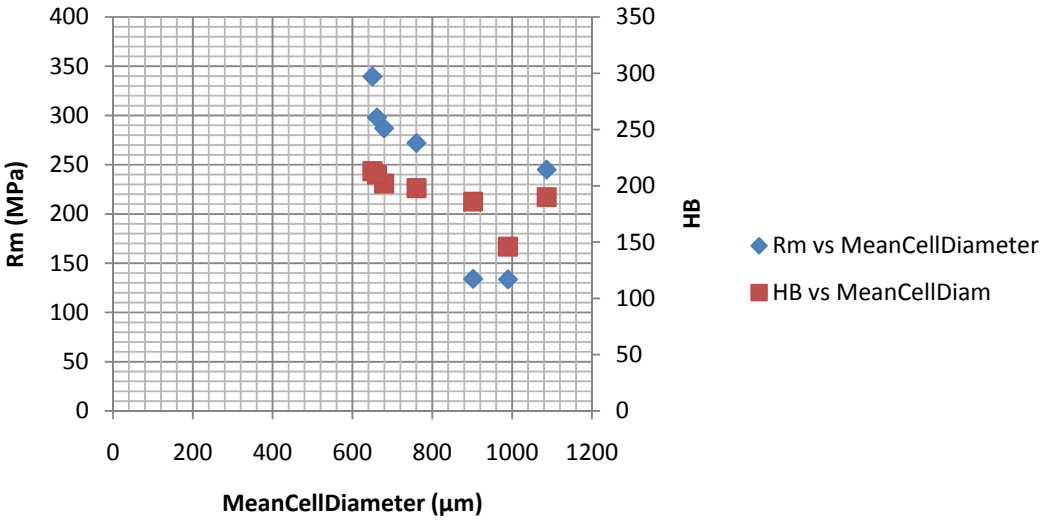

Figure 29. Cell diameter versus R_m and HB.

In Figure 29 the general decrease of mechanical properties with increasing cell diameter can be seen. The data point for diameters >1000 µm corresponds to material 2.2.2A.This is the only material with no inoculants. This should give the largest cells which are confirmed by the graph.

The R_m and Brinell hardness (HB) values differs but follows the same trend, since R_m measures a larger volume the probability of defect is larger and may be a reason for the differences.

The different cell sizes show different cell borders. The difference in strains between the cells and the borders is investigated with the DIC-technique by comparing the smallest and largest cell in melt 1 and 2. Starting with material 2.2.2A the strain-field and the appearance of the eutectic cells is depicted in Figure 30.

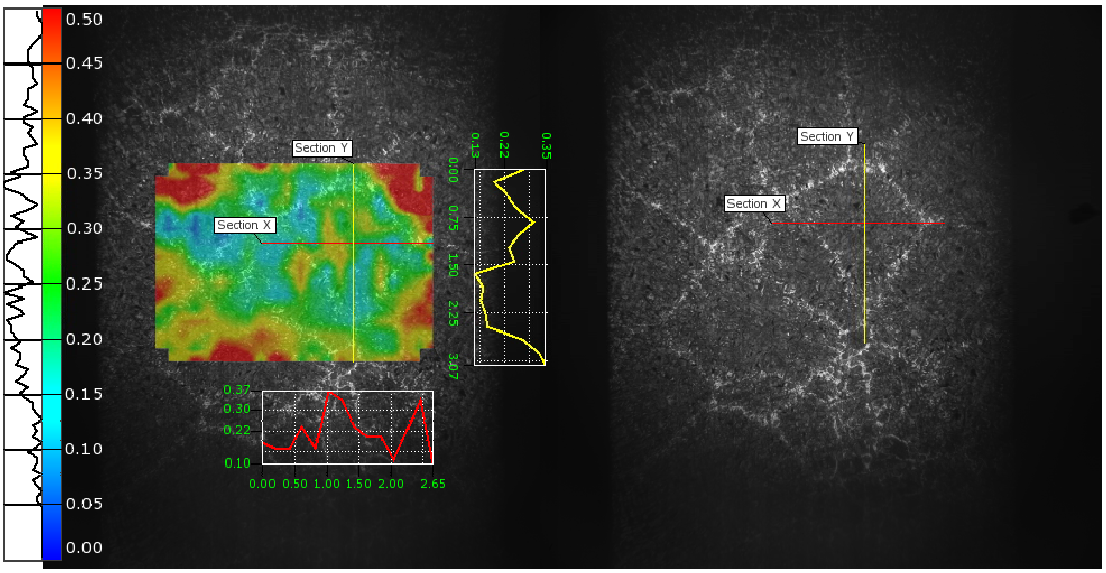

Figure 30. Material 2.2.2A. The image focuses on the strains in and around the eutectic cells at 150 MPa applied global stress. Sections X and Y are indicated.

Figure 30 shows two images next to each other. The left image contains two graphs, a strain-field and a combined histogram and color bar indicating which color corresponds to which strain. The right image shows the etched microstructure with section lines. The histogram indicates the relative frequency of the respective strains of the strain-field. The graphs show the distance on the x-axis (mm) and the strain level (%) on the y-axis. Their length corresponds to the real length in the image, and for that reason it is possible to follow the microstructure to see what part corresponds to what strain. It is important to notice that the section lines only show local values. If the yellow section line would have been moved further to the left in Figure 30, the graph would have shown even clearer values.

By following the yellow line (top-down) it can be seen that the strain increases when leaving the cell-boarder (white areas on picture) and going into the eutectic cell and decreases when leaving the cell (about 2 mm down, see yellow graph). Since graphite is the softest phase and occurs to the largest extent within the eutectic cell, this seems to apply as this will give rise to a strain concentration in the vicinity of the weak graphite. In the strain-field, local areas with higher strain concentrations occur. For material 2.2.2A the local concentration areas seems to mainly occur in the cell, with an exception to the lower left of the sectioned cell, where an local strain concentration area is crossing between the cells.

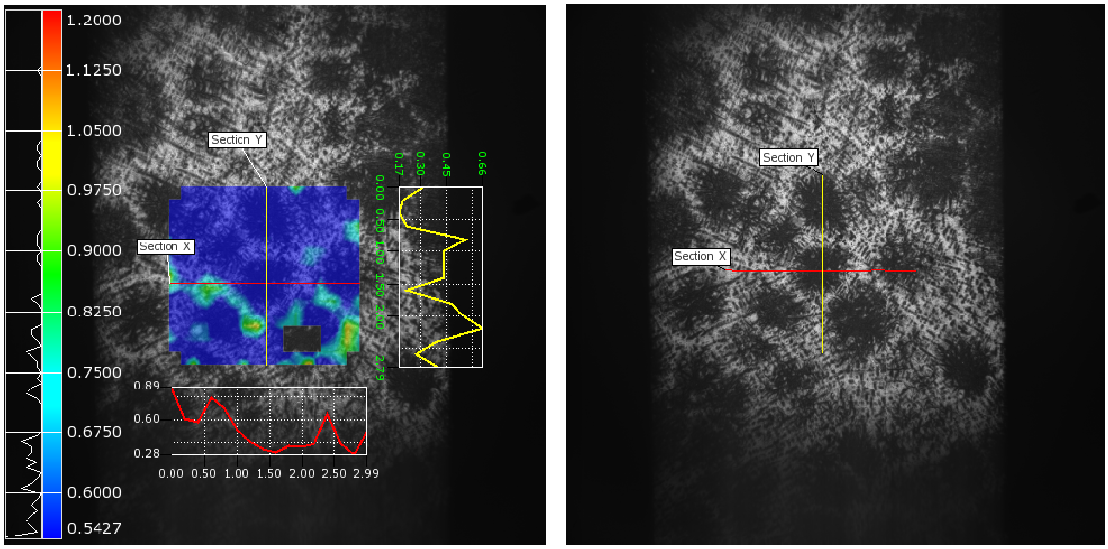

Figure 31. Strain field for material 2.6.2A at 150 MPa.

Compared to material 2.2.2A the cells are smaller in material 2.6.2A and the borders are wider as seen in Figure 31. In this case it can be concluded that this trend is contradictory to the previous where the highest strains are found at the cell borders. This can be seen more easily by following the yellow graph top-down, where it is observed that the lowest strains are found in the centre of the two cells studied. In addition to the smaller cells, material 2.6.2A has higher graphite roundness as an effect of the higher amount of N (a roundness of 0.15 compared to 0.13 for material 2.2.2A). Since the graphite is seen as cracks, the smoother crack end will reduce the stress concentrating effect. This may be one reason to the observed differences in strain concentration distribution.

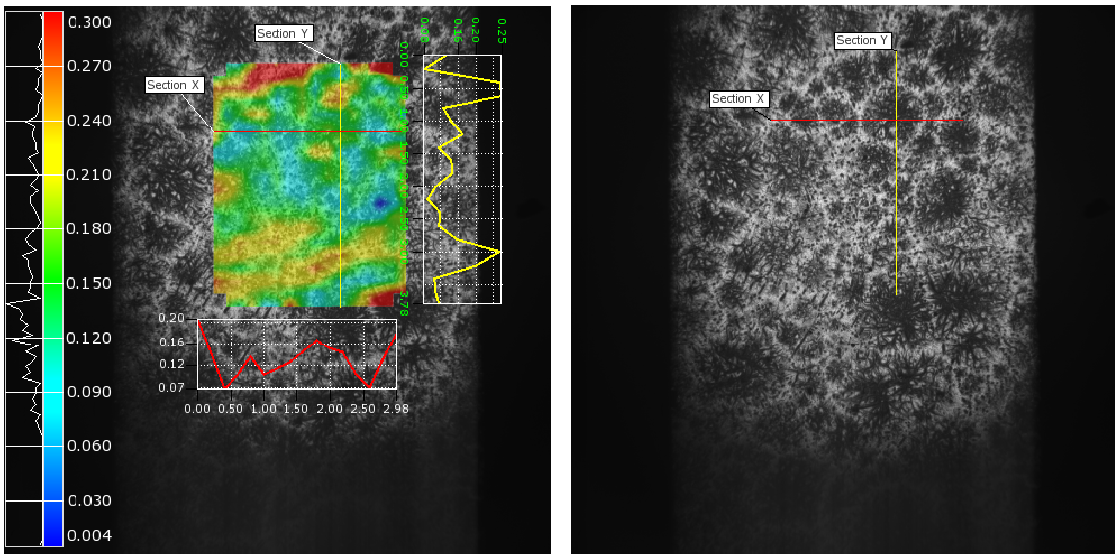

Figure 32. Strain field for material 1.2.2A at 150 MPa.

As shown in Figure 32 for material 1.2.2A the highest strains can be found within the cells. This material seems to have clusters of cells, which is easiest observed in the right image of

Figure 32. There are a higher amount of regions of the strain field that overlaps the cell borders than for the previously discussed materials (see cell border around the cell where the sections cross). The borders outside the clusters of cells are wider and areas of primary austenite are visible.

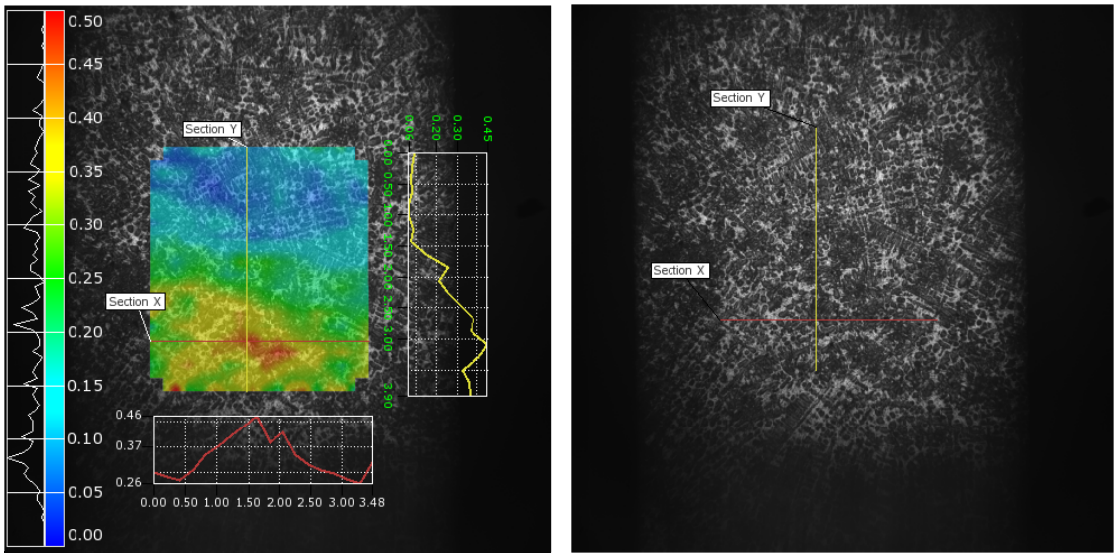

Figure 33. Strain field for material 1.11.2A at 150 MPa.

In Figure 33 it is harder to distinguish the cells from the rest of the microstructure. The cells seem to be small and the primary austenite appears in distinct patterns. The largest strains are found in the cells but the strains are more homogenous overall. Since material 1.11.2A has a low CE value the amount of primary austenite should be higher, which could be a reason for the more homogeneous strain-field.

7.4 Strain fields developed during cyclic tensile testing

All the samples were cyclically run in the tensile machine. The data from the tensile machine was used as input data to the Aramis reports. The test gave results typically like Figure 34 and was run according to Figure 20 (Chapter 6).

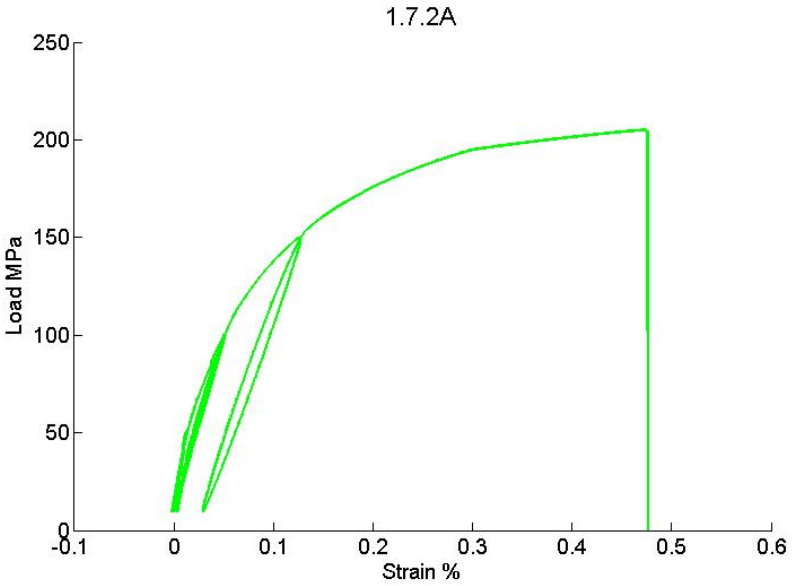

Figure 34. Cyclic stress strain curve for material 1.7.2A.

All the samples showed the same characterizations during run with Aramis. Below 50MPa there were no or little strains to the material. When the samples were run above 50 MPa, changes started to occur. The largest strain fields (Mises) were observed when the load was lowered again Figure 35.

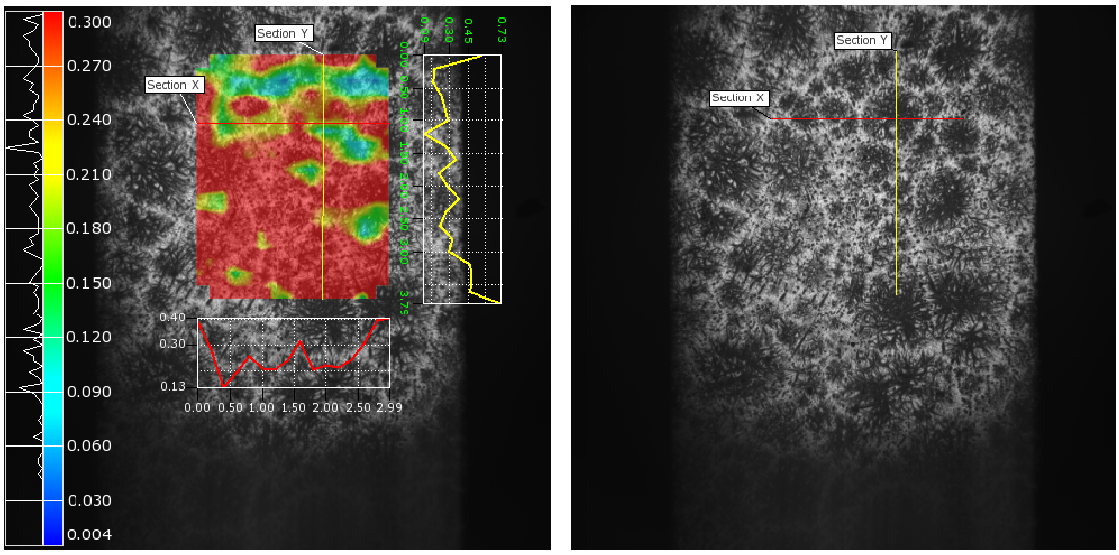

Figure 35. Image showing strain fields at 50 MPa for material 1.2.2A.

From Figures 32 and 35 it can be seen that the strain density differs between the different images. Figure 32 (at 150 MPa) showed clear strain patterns around the cells while figure 35 show a large red field. This is probably an effect of out of plane movement at low loads due to setting of the sample in the tensile test machine.

All samples showed higher strains at the same load in subsequent load cycles. This makes sense by looking at a stress strain curve, where each peak increases the elongation by giving rise to permanent strains. With a

more stable test set-up it could be possible to see what strain areas that reverse back to its original state and what areas that remain plastically deformed. In this way it should be possible to determine how the material and the inherent phases of the microstructure behave elastically and plastically. Since the out of plane effect (described earlier) was large at low strains it was hard to observe this difference. But some trends that seemed to occur were that a higher amount of strains remained in the eutectic cell borders while the center of the cells went back to its original strain levels. This indicates that the pearlitic borders are deformed plastically and that the graphite rich cells deform elastically, or more correctly the opening up of the graphite particles due to cracking are possible to close at unloading giving rise to a pseudo-elastic response of the graphite rich zones.

The highest strains within the strain-fields can otherwise be observed in areas with high amounts or large sized graphite. This is illustrated in the following images.

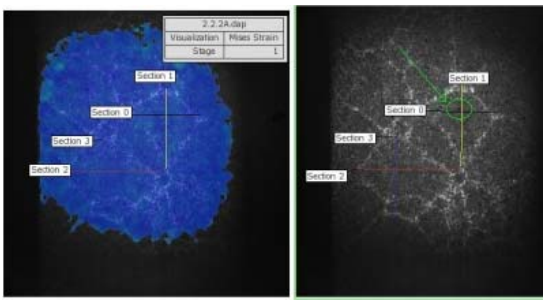

Figure 37. Image showing a large graphite field (marked by a green circle) for material 1.2.2A at zero load.

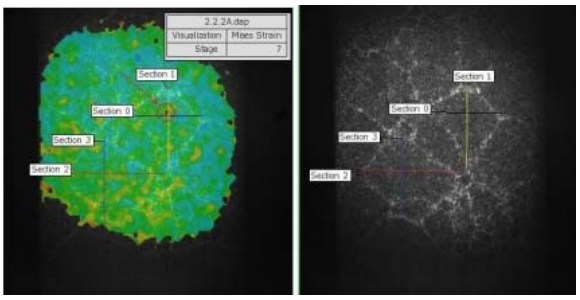

Figure 38. Same graphite field (marked by red circle) as in figure 36 but with an increased load of 30 MPa.

Figure 37-38 compares the strain fields over a graphite field for different loads. It can be seen that with large graphite like this the deformation is largest right at the graphite. Since graphite is the softest part of the matrix this makes sense and strengthens the method.

7.5 Limitations and possibilities with DIC

The light passing through the MPlan Apo objective was partly misled by focals of the microscope, creating an incomplete coverage of the CCD circuit area. For this reason part of the surface was masked in the software to reveal the useful area only.

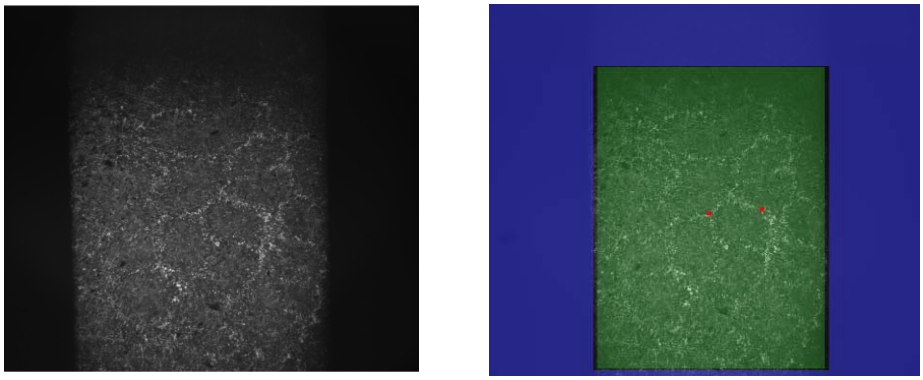

Figure 36. Unmasked image showing the surface of sample 1.7.2A. Right image showing the same image masked.

In this project the Y direction corresponds to the tensile direction and the X direction the perpendicular direction. To reduce the influence of the “noise” that occurs from movements in the sample at the start of a tensile test, a pre-force of approximately 10 MPa were used.

Since ARAMIS is using the natural pattern created with the color etching there can be some “bad” pattern, meaning that the system cannot distinguish a pattern due to lack in contrasts.

At late stages it can be hard for the system to detect the pattern. This can be due to large deformations, planar motions in any directions and bad start point for the calculation. Some of these losses can be seen in some of the samples at late stages as shown in Figure 37.

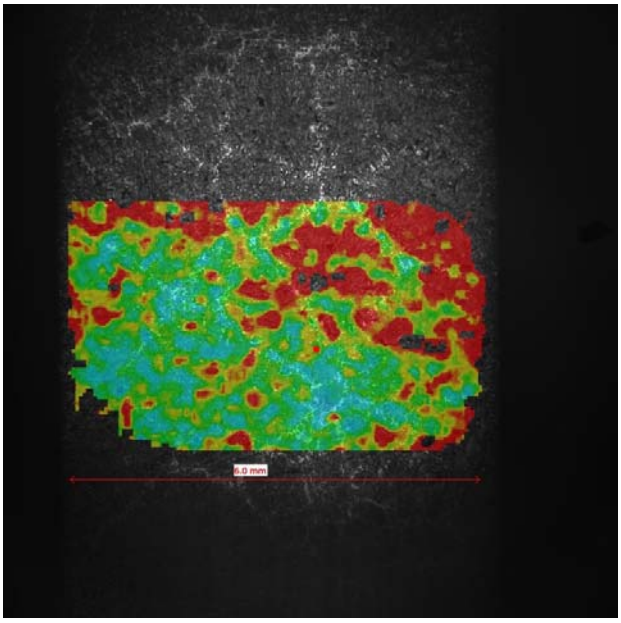

Figure 37.Material 1.2.2A showing calculation errors at 178 MPa. The errors are shown as black areas in the otherwise red areas.

These areas can be reduced by choosing better or additional starting points, adjust facet size and overlap, better masking and optimize camera to microscope lenses.

8 Conclusions

DIC method

One of the purposes of the thesis work was to see if and to what extent it was possible to use DIC to analyze strain fields on materials containing eutectic cells.
From the tests performed with the described techniques it could be concluded that it is possible to investigate strain-fields on a microscopic scale, different phases of cast irons and their strain response during loading and to investigate the effect of eutectic cells and primary austenite on the strain distribution.

Limitations with DIC

Since DIC analyses patterns in a grayscale image it is important to have good focus and a distinct pattern (natural or artificial).

The results from the program are hard to quantify and requires high degree of user knowledge e.g. setting the starting point wisely to be able to analyze the entire area.

The amount of data tends to be large which increases the risk of data losses.

Appearance of strain-fields and their local concentration fields

From the images containing strain-fields it was found that strains could be found at the cell borders and in the cells (the highest strains were found in the cells). For smaller eutectic cells, small elements of high strain concentrations were scattered throughout the strain field. An effect from different amounts and appearances of primary austenite on the strain field could be seen.

Dependencies

The different dependencies that were found by using the multivariate regression model showed the following dependencies:

- An increase in inoculants increases the materials strength
- An increase in inoculants decreases cell size and cell area
- An increase in inoculants decreases the cell spacing
- The strength of the cast iron material decreases with increasing cell size

Effect of chemical composition

The observed effects on the chemical composition were:

- The strength of the material increases with decreasing CE
- The tangent modulus increases with decreasing CE
- The amount of primary austenite increases with decreasing CE

9 Future work

In the future, it would be interesting to investigate the same material with a customized tensile testing machine, to optimize the mounting of the microscope and to use better illumination.
In this and previous studies the tensile testing machine and the setup of the microscope showed to affect the resolution of the results. For this reason, by improving the setup it should be possible to get a better spatial and strain resolution. This would make it easier to compare each sample and to draw conclusions regarding the details on a microscopic level. If a clear effect is shown this could also be investigated further with an SEM microscope to draw further conclusions regarding the cause.

10 Acknowledgements

I would like to express my gratitude to:

PhD Torsten Sjögren for his support and guidance throughout the entire work.

Professor Maria Knutson Wedel at Chalmers University of technology for guidance.

All SP personnel for being helpful, patient and friendly.

Scania CV AB for material and knowledge support.

11 References

1. **C.V, White.** *Gray iron, Properties and Selection; ASM handbook Vol 1* . s.l. : ASM international, 1990.
2. **Nunes, Rafael.** *Metals HandBook, Gray Iron, VOL 15 - CASTING* .
3. **G, Krauss.** *STEELS heat treatment and processing principles.* s.l. : ASM International, 1990. ISBN 0-87170-370-X.
4. **H, Svensson.** *Literature survey concerning the influence of elements on mechanical properties in gray cast iron.* s.l. : Swerea;Swecast, 2008.
5. **Bates, Bates C.E.** *Alloy Element Effects on Grey Iron Properties: Part II* . s.l. : AFS Transaction, vol. 154, p.889-912, 1986.
6. **A, Kagawa and T, Okamoto.** *Partition of alloying elements in freezing cast irons and its effect on graphitization and nitrogen blowhole formation.* Osaka : The institute of scintific and Industrial research Osaka University.
7. **F, Wilberfors and Ingvar, Svensson.** *graphite, The effect of nitrogen and inoculation on the tensile properties and microstructure of cast iron lamellar.* Södertälje; Jönköping : Scania CV AB; Jönköpings university, 2010.
8. **D.A, Porter and K.E, Easterling.** *Phase transformations in Metals and Alloys (second edition).* s.l. : CRC Press, 1981, 1992. 0-7487-5741-4.
9. **Campbell, John.** *Castings second edition.* Oxford : Butterworth-Heinemann, 2003. ISBN 0 7506 4790 6.
10. **Steve, Brich.** *Cast iron inoculation.* s.l. : Elkem.
11. **Steve, Birtch.** *Foundrisil 75 master.* Oslo, Norway : Elkem ASA Foundary Alloys, 2001.
12. **Lopez H, Fras E.** *Eutectic cells and nodule conunt-an index of molten iron quality.* 2010.
13. **ISO_945-1.** Microstructure of cast irons- Part1. *Graphite classification by visual analysis.* s.l. : International Organization for Standardization, 2008.
14. **Lennart, Elmquist and Diószegi, Attila.** *Influence of Solidification on the Primary Austenite Structure of Grey Cast Iron.* Jönköping : Department of Mechanical Engineering/Component Technology- Castings, Jönköping University, 2008. ISSN 1 404-0018.
15. **G.L, Rivera, R.E, Boeri and J.A, Sikora.** *Solidification of gray cast iron.* Argentina : Metallurgy Division INTEMA, 2003.
16. **Lennart, Elmquist.** *Defects formation during solidification in grey iron castings.* s.l. : Chalmers university of technology, 2009.
17. **Stefanescu, D.M. and S. Katz.** *Thermodynamic Properties of Iron-Base Alloys, Casting, Vol 15, ASM Handbook,ASM International, p 41–55* . 2008.
18. **E, Fras, M, Górny and H, Kapturkiewicz and Lopez.** *Eutectic cell and nodule count in cast irons.* Poland, USA : s.n., 2007.
19. **William, Callister .D.** *Materials science and engineering* . s.l. : Department of metallurgical engineering the university of Utah . ISBN-13 978-0-471-73696-7.
20. **L, Collini, G, Nicoletto and R, Konecna.** *Microstructure and mechanical properties of pearlitic gray cast iron.* s.l. : Material Science and Engineering , 2007.
21. **Donald, Zipperian.** *Chemical etching.* s.l. : PACE technologies, 2003.
22. **International, ASM.** *Gray Iron Castings, Casting, Vol 15, ASM Handbook, ASM International, pp 835–855.* s.l. : ASM International, 2008.
23. **M.R, Mitchell.** *Effects of graphite morphology, matrix hardness, and structure on the fatigue resistance of gray cast iron.* Detroit : Society of automotive engineers, 1975.
24. **R.C, Voigt and S.D, Holmgren.** *Crack initiation and Propagation in Gray and Compacted Graphite (CG) Cast Irons.* Kansas;Minnesota : AFS Transactions, vol. 98, 1990.
25. **Fredriksson, H., Sunnerkrantz, P.-A. and Ljubinković, P.** *Relationship between structure and thermal fatigue in cast iron.* s.l. : Maney publishing, 1988.
26. **T.J, Baker.** *The fracture resistance of flake graphite cast iron.* London : Department of Metallurgy and Material Science, Imperial College of Science and Technology, 1978.
27. **House, Random.** *Random House Webster's Unabridged Dictionary,Page 534, 971.* 2001. ISBN 0375425667.
28. **Svensson, Thomas.** *Statistik för experimentalister.* s.l. : SP Bygg&Mekanik, 2007.
29. **Michael., Sutton A, Jean-José, Orteu and Hubert, Schreier W.** *Image correlation for shape, motion and deformation measurements.* USA : Springer, 2009. ISBN 978-0-387-78746-6.

30. **J.G, Henzel and Keverian, Jr and J.** *Comparison of Calculated and Measured Solidification Patterns for a Varierty of Steel Castings.* s.l. : Trans. AFS, Vol 73, p 661-672, 1965.
31. **Sjögren, Torsten.** *Influences of the graphite phase on elastic and plastic deformation behavior of cast irons.* Jönköping : Department of Management and engineering Linköping University, 2007.
32. **R.N, Castillo and T.J, Baker.** *A Fracture mechanics to fatigue in flake graphite cast iron.* London : Department of metallurgy & material science Imperial collage .
33. **Lawn, Brian.** *Fracture of Brittle solids -second edition.* Cambridge : Press syndicate of the university of Cambridge, 1993. ISBN 0 521 40176 3.